12-3-2021

Study of Structural, Magnetic and Magnetocaloric Properties of (1-x) La0.7Ca0.3MnO3-xMO (M = Ni, Cu, Co) Nanocomposites.

Surendra Dhungana

STUDY OF STRUCTURAL, MAGNETIC, AND MAGNETOCALORIC PROPERTIES OF

(1-x) La$_{0.7}$Ca$_{0.3}$MnO$_3$-*x*MO (M = Ni, Cu, Co) NANOCOMPOSITES.

By

Surendra Dhungana

A Thesis

Submitted in Partial Fulfillment of

Requirements of Degree of

Master of Science

Major: Physics and Material Science

The University of Memphis

12/12/2021

Acknowledgement

I would like to express my heartfelt gratitude and respect to my advisor, Professor Dr. Sanjay R. Mishra. His constant guidance and support have played a key role in my masters journey at University of Memphis. He has enlightened me with his knowledge and impacted me with his approach to research.

I would also like to thank professor Dr. M.S. Jahan and Dr. Shawn Pollard for sparing their valuable and limited time to be in my thesis committee. My acknowledgement also goes out to all my professors throughout my Masters in University of Memphis, Dr. Thang Ba Hoang, Dr. Mohamed Laradji, Dr. Xiao Shen and the whole Department of Physics and Material Science.

My gratitude also goes out to Dr. Arjun K Pathak from The Buffalo State University, New York for assisting me with PPMS measurements for this work. Apart from this, I would like to thank my colleagues Dipesh Neupane and Jolaikha Sultana for their support and help with this work.

Finally, none of this would have been possible without the relentless support from my family and beloved friends. I owe everything I have accomplished so far to their presence and motivation.

Abstract

Manganites have shown potential application as magnetic refrigerants due to the exhibition of near room temperature magnetocaloric effect. High relative cooling power (RCP) values and the easy tunability of magnetic phase transition temperature (T_c), magnetic entropy change (ΔS_m), and RCP opens up a lot of possibilities for exploring better magnetocaloric materials. Reported literature shows doped manganites and composites with significant improvement in magnetocaloric properties.

In this work, we have synthesized *(1-x)* $La_{0.7}Ca_{0.3}MnO_3$-*x*MO (*x = 2.5%, 5%*; M = Ni, Cu, Co), magnetite-metal oxide nanocomposites using a simple autocombustion method. The structural and magnetic measurements have been made to explore the purity and the magnetocaloric properties of the sample. The x-ray diffraction data (XRD) of all the samples show the presence of a pure LCMO phase. The presence of metal oxides is further confirmed by energy-dispersive spectroscopy (EDS). The field Cooled magnetization curve shows that the material undergoes second-order PM-FM transition as we decrease the temperature. The obtained phase transition temperature (T_c) drops with the increasing content of metal oxides. The highest drop of T_c is observed from 258 K in pure LCMO to 166.6 K in LCMO-5%CoO. Isothermal magnetization curves for the composites also show PM-FM phase transition with the change in nature of the curve. The maximum magnetic entropy change (ΔS_{max}) is observed around T_c for all the samples, and it increases with the increase in the applied field. The largest drop in ΔS_{max} is observed from 8.77 $JKg^{-1}K^{-1}$ in pure LCMO to 3.24 $JKg^{-1}K^{-1}$ in LCMO-5%NiO. The most important parameter in quantifying the magnetocaloric behavior of the sample, RCP, is calculated, and it is found to increase linearly with the externally applied field. The RCP values increase with the increase in metal oxide content despite the decrease in ΔS_{max}. The highest value for RCP obtained is 266.89 JKg^{-1} in LCMO-5%CuO, which is a 23.4% gain from 213.13 JKg^{-1} for pure LCMO. The increase in RCP values with the increase

in metal oxide content signifies that we were able to tune and improve the magnetocaloric

behavior of LCMO by composite formation.

Table of Contents

List of Figures

LIST OF TABLES

Chapter 1 Introduction

1.1 Magnetic Materials

Magnetism was named after a city in Greece, Magnesia. The first discovered stone in Magnesia showing magnetic properties was Magnetite (Fe_3O_4), and the name magnet was set. William Gilbert first studied magnetism in the 1500s. In 1819, Ørsted studied the relationship between the electric and magnetic fields and concluded that one could generate another [1]. Later, Neel, Curie, and Weiss discussed the dependence of magnetic properties on temperature [2]. Throughout history, researchers and scientists have made efforts to utilize this magnetic property for various applications. They have been used for data storage, electronics, communication, general appliances, and many more. Given the wide range of practical applications, there have been numerous investigations searching for new materials that exhibit more desirable magnetic properties.

Magnetism is an intrinsic property of magnetic materials that depends upon the arrangement of magnetic spins. Based on how the spin particles align in the presence and absence of an external magnetic field, there are six types of magnetic materials,

1. Diamagnetic materials
2. Paramagnetic materials
3. Ferromagnetic materials
4. Ferrimagnetic materials
5. Antiferromagnetic materials and
6. Superparamagnetic materials

Diamagnetic materials have magnetic spin aligned randomly in all directions giving zero net magnetic fields. When external field is applied, the spins align in the direction opposite to

that of the external field resulting in the net magnetic field to be zero once again. In paramagnetic materials as well, the spins are randomly directed, producing a zero net magnetic field. But in the presence of an external magnetic field, the spins align in the direction of the field. These materials cannot retain the induced magnetic field when the external field is removed. The ferromagnetic materials have spins aligned parallel to each other, giving a net magnetic field even in the absence of an external magnetic field. Ferrimagnetic materials are very similar to ferromagnetic materials because they also have a net magnetic field even in the absence of an external field, but the difference is in the alignment of spins. In ferrimagnetic materials, the spins align antiparallel to each other, but the number of up and down spins is not equal, giving rise to a net magnetic field. Antiferromagnetic materials have an equal number of spins in opposite directions. This gives rise to a net magnetic field of zero. Superparamagnetic materials are essentially paramagnetic but with a small presence of ferromagnetic or ferrimagnetic spins. This behavior is seen in small grain sizes where the orientation of spins is very sensitive to temperature. The behavior of all of these particles in the presence and absence of external field can be seen in the figure below,
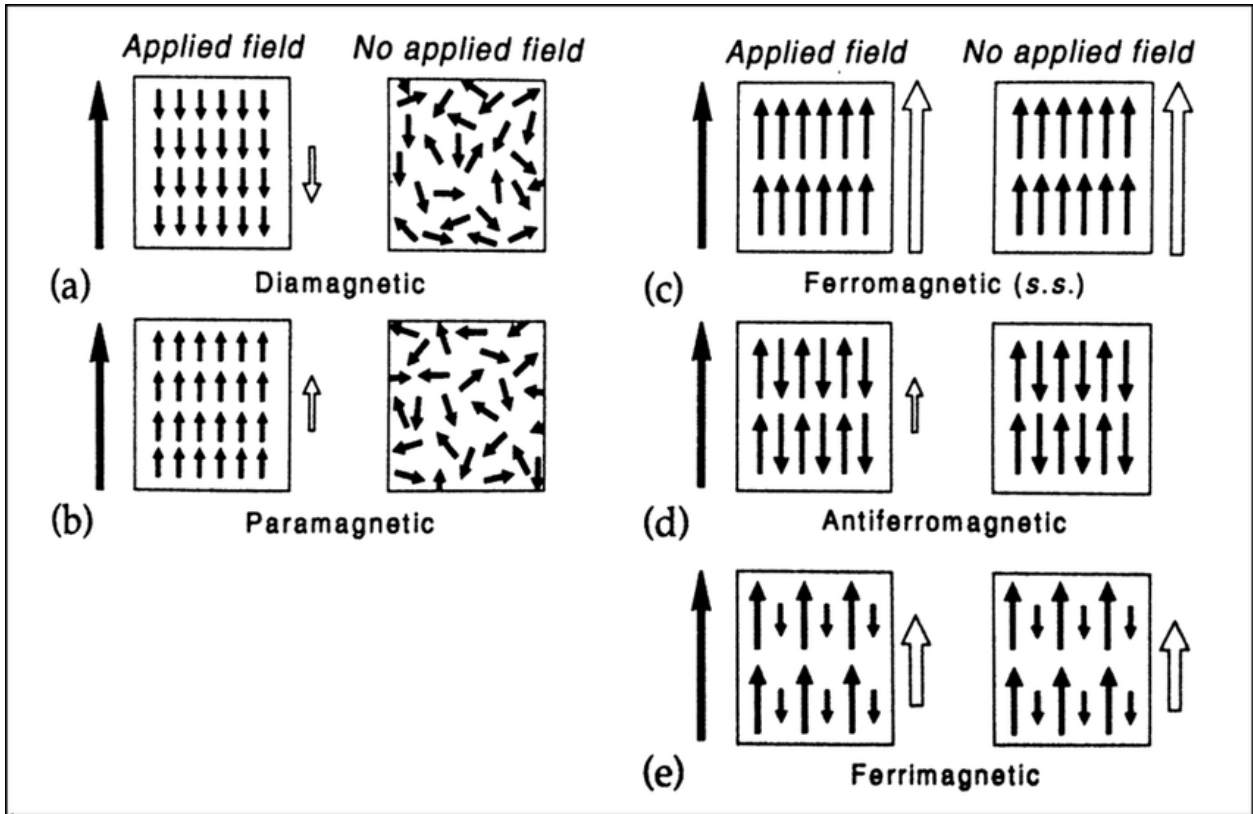
Fig. 1.1. Spin Orientation in different types of magnetic materials [3].

It is important to understand that the properties of all of these magnetic materials are temperature dependent as well. For example, ferromagnetic materials can become paramagnetic at higher temperatures due to thermal agitation. Also, paramagnetic materials can show different strengths of the net magnetic field at different temperatures.

1.2 MagnetoCaloric Effect (MCE)

The magnetocaloric effect was first discovered by Warburg in 1881 **[4]**. Debye **[5]** and Giauque**[6]** then provided a model to attain significantly low temperatures using magnetocaloric materials, and in 1933, Giauque and MacDougall were able to verify the model with an experiment. The magnetocaloric effect works based on the principle that a magnetic material undergoes an adiabatic change in temperature in the presence of an external magnetic field due to entropy conservation. The most practical application of this effect is magnetic refrigeration. Magnetic refrigeration has a lot of advantages over the

conventional gas refrigeration technique used abundantly today. It is more environmentally friendly since it does not produce harmful gases such as CFCs. On top of that, magnetic refrigeration is more efficient with a compact build.

When a magnetic material is exposed to an external magnetic field, the magnetic spin particles start to align in the direction of the external magnetic field. This decreases the magnetic entropy of the material as the randomness of the spin orientation decreases. To compensate for this loss of entropy, the material undergoes an adiabatic increase in temperature increases the lattice entropy. The material is then allowed to come back to the normal temperature by passing the heat through a sink. Then, the external magnetic field is removed, and magnetic spin particles start to randomize, increasing the magnetic entropy causing the material to undergo an adiabatic decrease in temperature. The complete cycle of magnetic refrigeration based on MCE is shown in the schematic below,
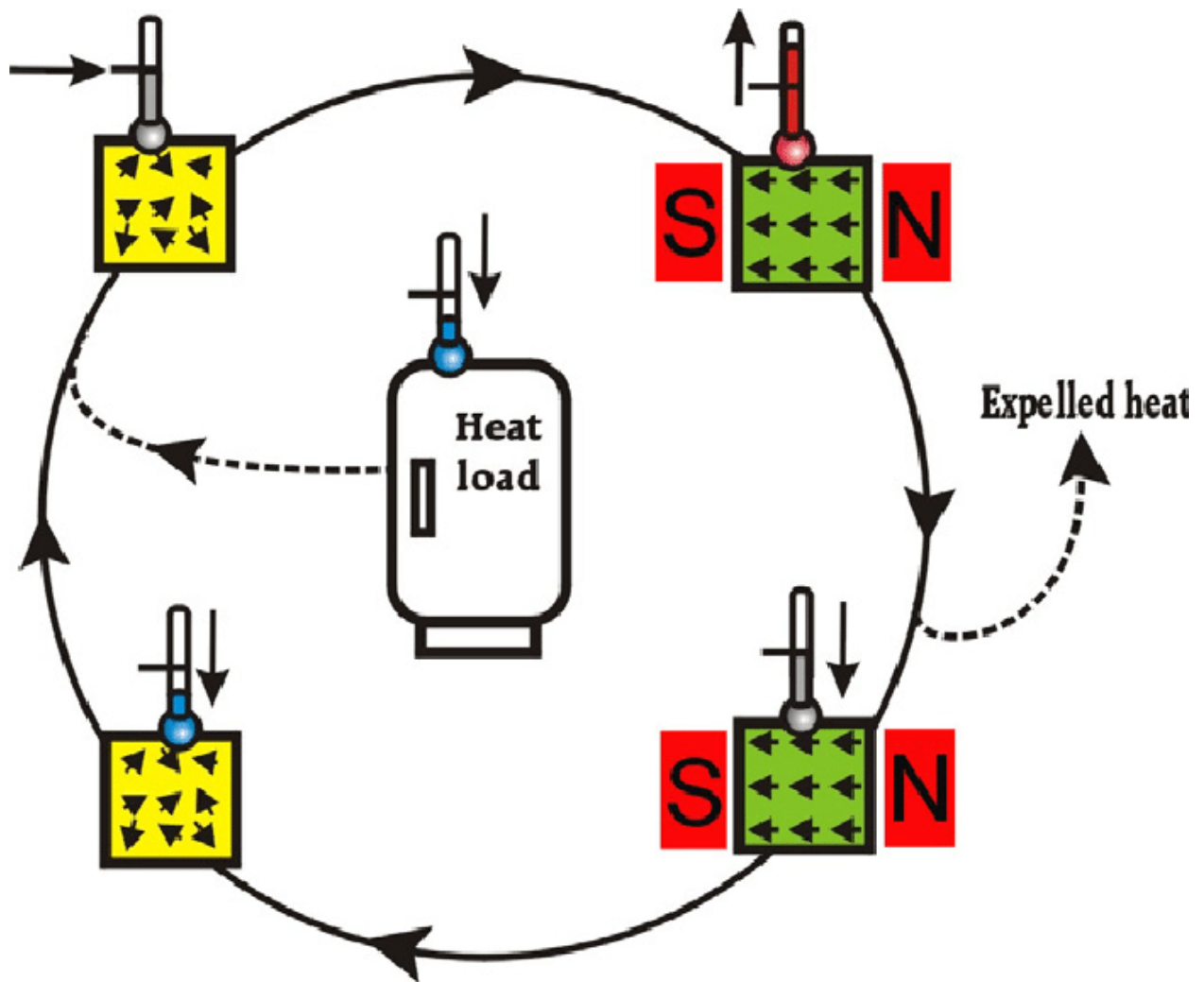
Fig. 1.2. Working Cycle of Magnetic refrigeration [7].

The change in lattice entropy, or in other words, the actual drop in temperature, depends upon the change in magnetic entropy. The higher the change in magnetic entropy, the higher will be the temperature change. This can be attained by using a material with entirely randomized magnetic spin particles, Paramagnetic materials. The problem with this is that paramagnetic materials usually do not undergo complete ferromagnetic ordering at room temperature. So, to see the desired significant change in magnetic entropy in such materials, they must be kept at a specific temperature.

The essential parameters quantifying the magnetocaloric behavior of the material are ferromagnetic to paramagnetic transition temperature (T_c), the magnetic entropy change

(ΔS_m), and the relative cooling power (RCP). The higher values of ΔS_m and RCP correspond to better magnetocaloric performance. RCP is the amount of heat transferred per ideal cycle. RCP is probably the most crucial parameter in quantifying magnetocaloric behavior. The higher value of RCP corresponds to the significant operational temperature of the material as a refrigerant. The transition temperature is favorable depending upon the application's purposes. The change in entropy is observed around the transition temperature. In other words, the magnetocaloric behavior can be harvested only around the transition temperature. So, for low-temperature applications, materials with lower transition temperatures are favorable, whereas, for room temperature applications, transition temperature should also be reasonably close to the room temperature.

1.3 Magnetocaloric materials

Different families of materials have been studied for potential application as a magnetic refrigerant. When it comes to room temperature magnetocaloric behavior, Gadolinium (Gd) is always taken as a reference as it is the first-ever material to show near room temperature magnetocaloric effect. Gd exhibited a maximum entropy change of around 9.4 $JKg^{-1}K^{-1}$ at a transition temperature of 293K for an externally applied field of 5T [8]. After this, multiple efforts have been made to find materials that can exhibit such high values of entropy change around room temperatures. Alloys, manganites, glass composites, and ferrites are the most studied materials where alloys and manganites stand out.

Alloys usually exhibit high magnetic entropy change and RCP. Some alloys have shown room near room temperature phase transition, but this varies greatly depending on the material. The synthesis of alloys is also an expensive and complicated process. Some alloys exhibiting outstanding magnetocaloric properties are given in Table 1.1.

Table 1.1. Magnetocaloric parameters of some alloys at 5T.

Material	T_c (K)	ΔS_{max} (JKg^{-1}K^{-1})	RCP (Jkg^{-1})	Ref.
Gd (bulk)	293	9.4	690	[8]
$MnCoGe_{0.995}In_{0.005}$	310	65	351	[9]
$CoMn_{0.9}Fe_{0.1}Ge$	290	34.9	240	[10]
$GdNiAl_2$	28	16	640	[11]
$Ni_{50}Co_2Mn_{33}In_{15}$	298	21.5	410	[12]
$(MnCoGe)_{0.89}(NiCoGe)_{0.11}$	300	24.1	257.4	[13]
$Mn_{1.1}Fe_{0.9}P_{0.79}Ge_{0.21}$	281.5	26.4	1138	[14]

Manganites are also widely studied for magnetocaloric study. They also exhibit significantly large entropy change and RCP. The transition temperature, similar to alloys, varies a lot. However, manganites have an advantage over alloys for the fact that their magnetocaloric properties, as well as the phase transition temperature, can be tuned effectively through doping and composite formation. The following table consists of some manganites showing remarkable magnetocaloric properties,

Table 1.2. Magnetocaloric parameters of some manganites.

Material	ΔH (T)	T_c (K)	ΔS_{max} (JKg^{-1}K^{-1})	RCP (Jkg^{-1})	Ref.
$EuTiO_3$	5	5.7	40.4	328	[15]
$HoMnO3$	7	75	8	540	[16]
$Pr_{0.5}K_{0.05}Sr_{0.45}MnO_3$	5	310	1.66	272.5	[17]
$Sm_{0.55}Sr_{0.45}MnO_3$	5	95	6.56	222.8	[18]
$La_{0.5}Ca_{0.5}Mn_{0.9}V_{0.1}O_3$	5	263	2.42	162.8	[19]
$NdMnO_3$	5	70	2.6	-	[20]
$LaMnO_3$	5	150	2.4	369	[21]
$La_{0.7}Ca_{0.3}MnO3$	1.5	267	1.2	65	[22]

It can be seen from Table 1.2 above that the rare-earth-based manganite of the form $REMnO_3$ exhibits better performance and has been widely studied.

1.4 Manganites

Perovskite was discovered by Gustav Rose in 1839 and named after a Russian mineralogist, Count Lev Aleksevich von Perovskite. Perovskites are a class of materials with the rudimentary composition of ABO_3. The manganites have proved to be a useful member of the perovskite family in magnetic applications. Manganites are perovskites where trivalent rare-earth cations such as La^{3+} occupy the A site and transition metal cations such as Mn^{3+} occupy the B site.

Let us take LaMnO3 as an example to explain the crystal structure. Here, the La^{3+} ions occupy the 8 corners of the cubic-like structure, Mn^{3+} ions are at the center of the cube, and oxygen ions occupy 6 face centers. The pseudo-cubic structure arises due to the tilt of the MnO_6 octahedron to maintain a low energy state. The tolerance factor for this crystal structure is given by,

$$t = \frac{\langle r_A \rangle + r_o}{\sqrt{2}(\langle r_B \rangle + r_o)} \tag{1}$$

where, $\langle r_A \rangle$ is the average ionic radius of A site

$\langle r_B \rangle$ is average ionic radius of B site

r_o is the ionic radius of Oxygen

The structure is stable for the range $0.8 < t < 1.0$. The tolerance factor 1 represents the cubic structure, $t < 0.96$ represents the orthorhombic phase, and $0.96 \leq t < 1$ represents the rhombohedral phase. The expected orthorhombic crystal structure for the $LaMnO_3$ is shown in the diagram below,
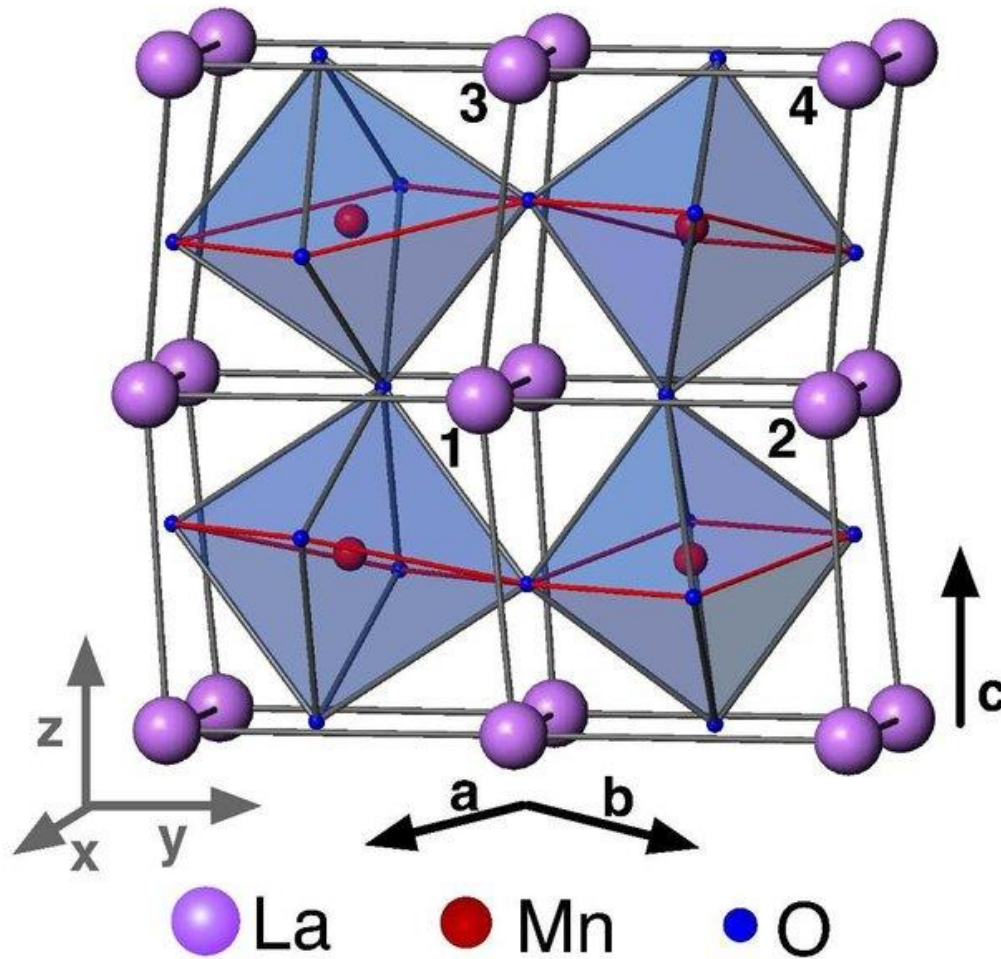
Fig. 1.3. Crystal Structure of LaMnO₃ Perovskite [23].

The manganites show a change in properties when atoms are doped in either the A or B site of the perovskite. The structural changes arise due to the change in average atomic radii as the dopant can have different ionic radii than the original constituent. This changes the spacing, bond length, and bond angle. The magnetic properties are also subjected to change by the introduction of a dopant. Doping impacts the magnetic interaction between cations.

Doping a cation with a different oxidation state than the original cation on A site will induce the double exchange interaction, which increases the ferromagnetic ordering. Substituting the transition metal cation on the B site suppresses the double exchange interaction and decreases the magnetization of the material. Also, antiferromagnetic super exchange interaction can

arise due to B site doping in some cases, which gives rise to magnetic inhomogeneity and further hampers the magnetic properties.

The composite formation can also alter the magnetic properties of a manganite. Forming a composite with antiferromagnetic metal oxides can result in magnetic inhomogeneity. The coexistence of the ferromagnetic phase of the perovskite and antiferromagnetic phase of metal oxides can result in a drop in net magnetization.

1.5 $La_{0.7}Ca_{0.3}MnO_3$-MO

The pure $LaMnO_3$ is antiferromagnetic in nature below Curie Temperature (T_c = 150 K [21]), meaning an equal number of the spin particles are aligned in opposite directions. The doping of divalent metal ions such as Ca^{2+}, Sr^{2+}, etc., on the A site, has shown antiferromagnetic to ferromagnetic transition below T_c. The replacement of trivalent La^{3+} ions by divalent ions gives rise to the double-exchange interaction between different oxidation states of Mn bonded through oxygen, increasing the ferromagnetic ordering of the magnetic spin particles. Double-exchange interaction occurs when two metal cations of varying oxidation states are bonded through a third non-magnetic anion.

For example, in $La_{0.7}Ca_{0.3}MnO_3$, the Mn ions exist in Mn^{3+} and Mn^{4+} oxidation states. So, the Mn-O-Mn bond experiences double-exchange interaction. In this case, the oxygen atom donates an electron to the electron deficient Mn^{4+} ion creating a vacant spot in oxygen. This is filled by Mn^{3+} cation. This interchanges the oxidation state of the Mn ions in the Mn-O-Mn bond, and the cycle repeats again. This is better represented by the schematic given below in Fig. 1.4.
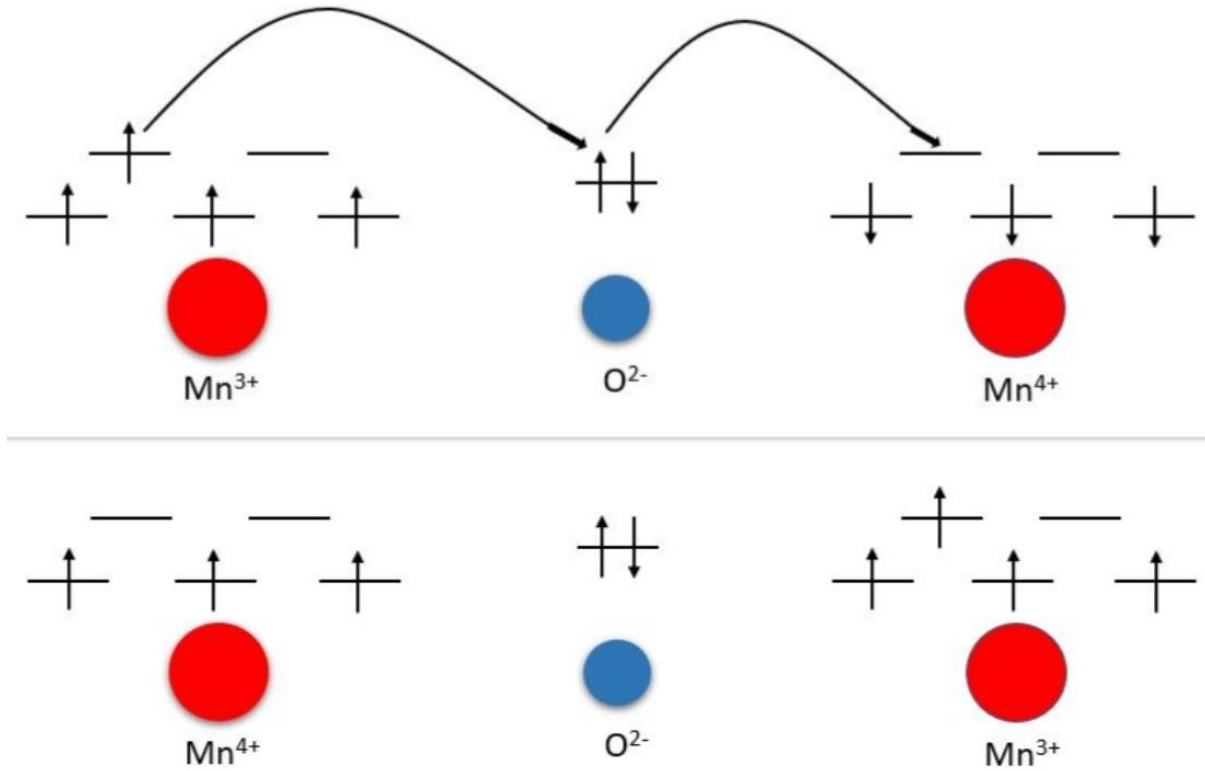
Fig. 1.4. Schematic of double exchange interaction in Mn-O-Mn.

This jump of an electron from one cation to other leads to the alignment of spins on the recipient cation following Pauli's principle; hence, ferromagnetic ordering is induced.

$La_{0.7}Ca_{0.3}MnO_3$-MO composites can undergo multiple phenomena, which leads to change in structural and magnetic properties of the material. The metal oxide (MO) composites are most likely to deposit on the grain boundaries of the perovskites. These metal oxides are usually cubic and are antiferromagnetic in nature. The deposition of such an antiferromagnetic phase in the grain boundaries can give rise to magnetic insulation, ultimately decreasing the magnetic performance. Magnetic inhomogeneity can also arise due to the coexistence of ferromagnetic perovskite and antiferromagnetic metal oxides resulting in altering the magnetic properties.

Chapter 2 Literature Review

2.1 Manganites

Biswas et al. synthesized bulk and nanoparticle $LaMnO_3$ crystals using the sol-gel method. The magnetocaloric behavior was significantly improved in the nanoparticles, which is attributed to the existence of a superparamagnetic phase around PM-FM transition temperature in nanoparticles. The transition temperature also slightly increased in the case of nanoparticles. [21]

Iqbal et al. synthesized $LamNO_{3+\delta}$ using the solid-state method. The trigonal crystal structure with the hexagonal setting was observed, which showed relatively low ΔS_{max}. [24]

Tola et al. synthesized $LaMnO_3$ nanoparticles with a sol-gel method using Polyvinyl alcohol (PVA). The magnetic properties were improved, which is credited to the presence of excess oxygen increasing the double exchange interaction between Mn ions. However, ΔS_{max} values were very low, which was reasoned with the loss of long-range magnetic ordering and the presence of magnetic disorder on the surfaces of nanoparticles. The operational range was found to be largely due to the magnetic inhomogeneity because of the coexistence of ferromagnetic and antiferromagnetic phases. [25]

Dyakonov synthesized $REMnO_3$ (RE = Nd, Pr) using the sol-gel method at different temperatures producing crystals in different scales. The magnetization was lowered with a smaller grain size. Also, the PM-FM transition temperature and the Neel temperature were lowered by grain refinement. [26]

Midya et al. synthesized and studied the magnetic anisotropy and magnetocaloric effect in $RMnO_3$ (R = Dy, Tb, Ho, Yb) crystals. They found that in these manganites, the magnetic entropy change was sensitive to the axis of magnetization, and they exhibited both positive

and negative MCE depending on the direction of the applied filed. They concluded that the magnetocaloric effect was relatively large in all of the samples except $YbMnO_3$ and the samples were potential materials for magnetic refrigeration. [27]

Balli et al. synthesized $DyMnO_3$ using a solid-state reaction and studied the rotational magnetocaloric properties. It was found that $DyMnO_3$ exhibits a great change in magnetic entropy when the applied magnetic field is along the easy axis as compared to the hard axis. This creates a different technique for magnetic refrigeration rather than the conventional magnetization-demagnetization process by simply rotating the sample. [28]

Balli et al. synthesized $TbMnO_3$ using the floating zone technique. It was reported that the rotational magnetocaloric effect (RMCE) was very high in this material. The magnetic entropy change along the hard axis was double as compared to that along the easy axis. [29]

Swamy et al. synthesized $YMnO_3$ using solid-state reaction and obtained a spin glass type PM-FM transition which is due to spin cantering. The ΔS_{max} values were increasing with the increase of the applied field, and RCP also increased as the peak was broadened with higher magnetic fields. [30]

Chandra et al. synthesized bulk and nanoscale $NdMnO_3$ using the sol-gel method. The ΔS_{max} vs. T graph showed two peaks for nanoparticles but only one peak for the bulk particles. The loss of this peak at the higher temperature value is credited to the coexistence of antiferromagnetic (AFM) and ferromagnetic (FM) phases in the bulk sample. [20]

2.2 Doped Manganites

Das et al. synthesized Na doped $LaMnO_3$ using solid-state reaction. The PM-FM transition temperature was increased in the Na doped $LaMnO_3$ which is due to the increase in double exchange interaction between Mn ions. The ΔS_{max} value also increased with doping. The

effect of pressure was also studied, and it was found that applying external pressure also enhances magnetocaloric properties. **[31]**

Afify et al. synthesized Ag-doped $LaMnO_3$ using the wet chemical method and studied the PM-FM transition of the series of samples. It was observed that the transition temperature increased with the content of silver. This is because of the induced double exchange interaction in the samples. Also, the broadening of the curve was observed, which is attributed to the magnetic inhomogeneity caused in the grain boundaries. **[32]**

Kolat et al. synthesized $La_{1-x}Bi_xMnO_3$ (*x = 0.01, 0.03, 0.06, 0.1, 0.2*) using solid-state reaction. The compounds showed a decrease in PM-FM transition temperature with an increase in the content of Bi as opposed to other literature. This is attributed to the change of order of PM-FM transition from first to second order with the increasing content of Bi. **[33]**

Kallel et al. synthesized $La_{0.7}Sr_{0.3}Mn_{1-x}Cr_xO_3$ (*x=0.00, 0.20, 0.40 and 0.50*) using solid-state reaction. The ΔS_{max} values and the PM-FM phase transition temperature decreased with the increase in the content of Cr, which is attributed to the suppression of double exchange interaction and enhancement of superexchange interaction. They noted a significant drop in T_c with a minimal drop in ΔS_{max} for the *x=0.20* sample. **[34]**

Phan et al. synthesized $LaMn_{0.9}Fe_{0.1}O_3$ using the conventional solid-state method and observed a decrease in ΔS_{max} value. This is attributed to the enhancement of both FM double exchange interaction and AFM superexchange interaction resulting in magnetic inhomogeneity. **[35]**

Rehman et al. synthesized $Pr_{1-x}Ba_xMnO_3$ (*x = 0.2, 0.3, 0.4, 0.5*) using ceramic method. The saturation magnetization, PM-FM phase transition temperature, and magnetic entropy increased with the increase in Ba content up to 0.4. This is attributed to the enhancement of double exchange interaction due to the increasing number of ferromagnetic domains. The *x =*

0.5 sample showed a disruption in the trend with decreasing saturation magnetization, PM-FM phase transition temperature, and magnetic entropy due to the antiferromagnetic superexchange interaction as the antiferromagnetic domains increased in the sample. [36]

Biswas et al. synthesized $Pr_{0.75}Li_{0.25}MnO_3$ using a wet chemical mixing route and studied the structural and magnetocaloric properties of the sample. The enhancement in ΔS_{max} was observed which is due to the presence of mixed FM-AFM phase around transition temperature and spin glass transition. [37]

Hcini et al. synthesized $Nd_{0.67}Ba_{0.33}Mn_{1-x}Fe_xO_3$ using solid-state method. The ΔS_{max}, T_c, and RCP all decreased with the increasing content of Fe. This is accounted by the decreases in double exchange interaction and increase in superexchange interaction between Fe and Mn ions. The increase in magnetic inhomogeneity also contributes to the lowering of the parameter values. [38]

Baazaoui et al. synthesized $Ln_{0.67}Ba_{0.33}Mn_{1-x}Fe_xO_3$ (Ln = La or Pr) and recorded an increase in the ΔS_{max} values due to Ba doping and a decrease in ΔS_{max} and transition temperature values due to the presence of Fe. The RCP was consistently high for all the samples, and the transition temperature was also ever so slightly affected by Ba doping. [39]

2.3 Manganite Composites

El Boukili et al. synthesized *(1-x)* $La_{0.6}Ca_{0.4}MnO_3$/xMn_2O_3 composites using solid-state reaction. The transition temperature remained unchanged with composite formation, but a decrease in ΔS_{max} and an increase in RCP were recorded with the increasing content of Mn_2O_3 in the structure. [40]

Anwar et al. synthesized $La_{0.7}Sr_{0.3}MnO_3$/Co_3O_4 and $La_{0.7}Ca_{0.3}MnO_3$/Co_3O_4 composites using solid-state reaction. The transition temperature and the ΔS_{max} values dropped, but the RCP value increased by the introduction of Co_3O_4 in the perovskite. This is credited to the

antiferromagnetic nature of Co_3O_4 inducing magnetic inhomogeneity in the ferromagnetic perovskite. [41]

Nasi et al. synthesized $La_{0.6}Sr_{0.4}MnO_3/ x(Sb_2O_3)$ composites using solid-state reaction. The ΔS_{max} and RCP values dropped as compared to the pure perovskite, which is due to the decrease in delocalization of the electron, which minimized the double-exchange interaction. The transition temperature, however, remained constant, implying that the Sb_2O_3 phase-only remains at the grain boundaries and does not react with $La_{0.6}Sr_{0.4}MnO_3$ to include within the perovskite structure. [42]

Gavrilova et al. synthesized *(1 − x)* $La_{0.7}Sr_{0.3}MnO_3/x$NaF composites using solid-state reaction. The magnetic entropy and transition temperature have dropped due to the introduction of the secondary NaF phase, which is the contribution of grain size reduction. The RCP values, however, did not change significantly due to the magnetic inhomogeneity. [43]

Neupane et al. synthesized $La_{0.45}Nd_{0.25}Sr_{0.3}MnO_3/MO$ (MO=CuO, CoO, and NiO) composites using autocombustion method. The ΔS_{max} values have increased while the RCP has decreased with the increasing amount of metal oxides, attributed to the increase in grain size. Also, the proximity of the phase transition temperatures of the perovskite and the metal oxides have shown an impact on the change of ΔS_{max} and RCP values. [44]

Maalam et al. synthesized $La_{0.45}Nd_{0.25}Sr_{0.3}MnO_3/5CuO$ using solid-state reaction and were able to increase the ΔS_{max} by the addition of the CuO phase. This is because of the observed grain growth by the introduction of the secondary phase. The transition temperature also increased, but the RCP value decreased due to the sharpening of the FM-PM transition. [45]

Ezaami et al. synthesized *(1-x)* $La_{0.7}Ca_{0.2}Sr_{0.1}MnO_3/x$$La_{0.7}Ca_{0.15}Sr_{0.15}MnO_3$ ($0 \leq x \leq 1$) composite samples using solid-state method. The dual-phase transition was observed due to

the existence of both phases. The dual peak of ΔS_{max} also verified the coexistence of phases. The values of ΔS_{max} were dominated by the content ratio. The RCP increased with the composite formation as the increase in magnetic inhomogeneity increased the broadness of the ΔS_{max} vs. T peaks. [46]

Nassri et al. synthesized $La_{0.6}Ba_{0.2}Sr_{0.2}MnO_3$ *(1−x)*/Co_2O_3-*x* using solid-state reaction. Two transition temperatures were obtained, which gave rise to two ΔS_{max} peaks as well. The higher transition temperature and ΔS_{max} values dropped with the increase in Co_2O_3 content which is attributed to the magnetic inhomogeneity. The RCP values increased with the increase in Co_2O_3. [47]

Ahmed et al. synthesized $La_{0.7}Ba_{0.3}MnO_3$ *(1-x)*/Al_2O_3-*x* using solid-state reaction. The phase transition temperature and ΔS_{max} decrease with the increasing content of Al_2O_3, and the RCP value increases. This is attributed to the deposition of Al_2O_3 on the grain boundaries and the decrease in volume fraction of the pristine perovskite. [48]

Ahmed et al. synthesized $NdSrMnO$/CrO_3 composites using solid-state reaction. The PM-FM transition temperature has decreased with the increasing amount of CrO_3 in the composite. The composite system showing first-order phase transition yielded a high value for ΔS_{max}, but those undergoing second-order phase transition gave higher values for RCP due to the broadening of the ΔS_{max} vs T peak. [49]

Fkhar et al. synthesized $Pr_{2/3}Sr_{1/3}MnO_3$-CuO using solid-state reaction. ΔS_{max} increased with the increase in CuO content, whereas the phase transition temperature and RCP decreased. This is attributed to the antiferromagnetic nature of the CuO, and the first-order phase transition observed in the perovskite. [50]

Chapter 3 Hypothesis and Approach

3.1 Rationale

From the literature review, it is understood that we can tune the magnetocaloric properties of manganites by doping either on the A or B site of the perovskite and forming composites. The doping causes a change in structure due to variation in ionic radii, which changes the properties of the material. Composite formation causes magnetic inhomogeneity, which impacts the net magnetic behavior of the material.

The intent of this work is to understand and improve the magnetocaloric performance of Lanthanum-based manganite through composite formation. Literature shows that composite formation causes the decrease in the maximum magnetic entropy change (ΔS_{max}) but increases the Relative Cooling Power (RCP) by increasing the operating temperature range for the magnetocaloric effect. Also, the composite formation can help tune the PM-FM transition temperature. Moreover, literature abundantly shows the use of solid-state reactions for the synthesis of manganites and composites. The autocombustion route for the synthesis of manganites and composites has not been recorded widely. So, we plan to form the composites using autocombustion synthesis and see if that changes magnetic parameters.

Table 3.1 presents the important magnetocaloric parameters of some manganite composites for reference.

Table 3.1. Magnetocaloric parameters of some manganite composites.

Material	Field	T_c	ΔS_{max}	RCP	Ref.
$La_{0.6}Ca_{0.4}Mn_2O_3$-20%MnO_3	5	260	5.21	235	[40]
$La_{0.6}Sr_{0.4}MnO_3$-7%Sb_2O_3	5	371	3.38	165.62	[42]
$La_{0.45}Nd_{0.25}Sr_{0.3}MnO_3$-5%$CuO$	5	297	3.21	221	[44]
$La_{0.7}Sr_{0.3}MnO_3$-5%NaF	9	365	4.24	369	[43]
$Nd_{0.6}Sr_{0.4}MnO_3$-2%CrO_3	3	278	1.65	122.1	[49]
$Pr_{0.67}Sr_{0.33}MnO_3$-10%CuO	5	224	5.05	246	[50]

Based on the literature, we have selected single calcium doped Lanthanum manganate with the composition, $La_{0.7}Ca_{0.3}MnO_3$ as our perovskite. $La_{0.7}Ca_{0.3}MnO_3$ has recorded high ΔS_{max}, and the PM-FM transition temperature is also around room temperature. High ΔS_{max} is necessary since composite formation decreases this value in compensation of increasing RCP, but we still want this to be significant for operational purposes. We have selected antiferromagnetic metal oxides such as NiO, CuO, and CoO to form composites with the perovskites. NiO, CuO and CoO are antiferromagnetic with respective Neel temperatures of 525 K, 230 K and 291 K [44]. This antiferromagnetic phase produces magnetic inhomogeneity and enhances magnetocaloric properties as well as helps tune the phase transition temperature [44, 45, 50].

3.2 Statement

The proposed works studies and compares the magnetocaloric behavior of the *(1-x)* $La_{0.7}Ca_{0.3}MnO_3$-*x*MO (*x* =0.0%, 2.5%, 5% by weight; M = Ni, Cu, Co) composites.

3.3 Objectives

1.   To synthesize the $La_{0.7}Ca_{0.3}MnO_3$-xMO (x = 0.0%, 2.5%, 5%; M = Ni, Cu, Co) composites using autocombustion technique.

2.   To study the structural properties of the composite and determine lattice parameters, crystalline size, and atomic composition.

3.   To study the magnetocaloric properties of the composites and determine parameters such as maximum magnetic entropy change (ΔS_{max}) and relative cooling power (RCP).

Chapter 4 Experimental

4.1 Synthesis

The autocombustion method is chosen for the synthesis of said nanocomposites. This is a widely used method for the synthesis of nanoparticles as it is very convenient, cheap, and rapid **[52]**. In addition to this, we can produce high purity products in virtually any shape or size with this method and the reaction is self-sustaining as well as the products are highly effective for environmental remediation **[51, 52, 53]**. In this method, the precursors such as nitrate salts are mixed in the desired solvent (e.g., DI water) with a fuel (e.g., citric acid, glycine, etc.) to form a homogeneous solution. The solution is then allowed to dry into a gel. The temperature of this gelation process depends upon the solvent used. The temperature suddenly increases to ignite the reaction between the precursors, and the desired nanoparticle is obtained. The obtained solid product is then ground and calcined to remove any impurities present. The temperature of calcination depends upon the initial chemicals.

4.2 Structural Characterization

X-ray Diffraction (XRD) technique is used for the initial structural characterization of the sample. Bruker D8 Discover diffractometer is used. The x-Ray diffraction works on the basis of Bragg's Law of diffraction. Bragg's law states that when the wavelength of the incident x-ray is comparable to atomic spacing, the x-ray scattered from the lattice of the crystal structure undergoes constructive interference. This phenomenon only takes place for specific values of incident angle, d-spacing, and the wavelength of the incident x-rays.

Fig. 4.1. Bragg's Law of Diffraction.

Mathematically, Bragg's Law is expressed as,

$$2dsin\theta = n\lambda \qquad (2)$$

where,

d = spacing between two successive layers of atoms

θ = glancing angle (measured from the surface)

λ = wavelength of the X-ray used

n = order of diffraction

During x-ray diffraction, first-order diffraction is considered, and the wavelength of the x-ray used in our experiment was 1.54 Å.

Further, the obtained XRD pattern was analyzed to obtain crystalline parameters. First, the obtained data was also used to find the crystallite size using Scherrer's method. Individual peaks are studied to obtain the crystallite size of the sample.

According to Scherrer's method, the crystallite size of a sample is given by the formula,

$$D = \frac{k\lambda}{\beta cos\theta}$$

(3)

where,

k = dimensionless shape factor = 0.94

λ = wavelength of X-ray used

β = Full Width at Half Maxima (FWHM) of the peak

θ = angle at which the peak is observed

Halder-Wagner-Langford (HWL) plot was also used to find the crystalline size and lattice strain in the sample. The HWL equation is as follow,

$$\left(\frac{\beta^*}{d^*}\right)^2 = \frac{1}{T}\left(\frac{\beta^*}{d^{*2}}\right) + \frac{\varepsilon}{2}$$

(4)

where,

$\beta^* = \{\beta \cos(\theta)\}/\lambda$

$d^* = \{2 \sin(\theta)\}/\lambda$

$1/T = D$ = Crystalline size

$\varepsilon/2$ = Lattice strain

Scanning Electron Microscopy (SEM) was used to study the shape and morphology of the samples. SEM is used to image significantly smaller particles where visible light is not able to trace an image. SEM uses electrons instead of visible light to trace the image. The SEM detects the secondary electrons emitted from the sample, upon being excited from the atoms of the sample using primary electron beam. Magnetic lenses are used to focus the electron beam onto the sample, and the receiver collects secondary electrons. The back scattered electrons (BSE) scattered from the deeper regions of the sample, and secondary electrons

22

(SE) scattered from the surface of the samples are generally collected to provide a detailed image of the sample.

Energy Dispersive Spectroscopy (EDS) is used to further confirm the chemical composition of the synthesized sample. When an electron strikes a sample, it strikes the inner shell of the sample, ejecting the electron creating a vacant hole in the inner shell. To stabilize, an electron from the outer shell jumps to the inner shell, and energy is released in the form of the x-rays and is collected by a detector. The energy dispersed is unique to each element, and the presence of an element can be identified. A complete mapping of such energy spectra can be used to determine the atomic percentage in the sample. Thus, we can determine the chemical composition of the sample.

4.3 Magnetic and Magnetocaloric Characterization

To determine the magnetic and magnetocaloric properties of the samples, Dynacool Quantum Design Physical Property Measurement System (PPMS) is used. PPMS measures the magnetization of the sample exposed to different changing parameters such as temperature and applied magnetic field. The external applied field was changed from 0 T to 5 T whereas the temperature change was about 100 K around the vicinity of phase transition temperature.

First, temperature-dependent magnetization (M) of the samples is measured. This helps us observe the ferromagnetic to the paramagnetic transition of the sample. The data obtained can be differentiated to get dM/dT vs. T graph. The peak of this plot gives us the phase transition temperature.

After this, the sample's magnetization is measured by changing the applied magnetic field (H) at different temperatures. The curve exhibits paramagnetic nature above the PM-FM phase transition temperature (T_c). The magnetization shows a linear rise with the increase in an external magnetic field. At temperature values lower than T_c, the curve exhibits a

23

ferromagnetic nature where the saturation of magnetization is observed at higher values of the external magnetic field.

Further, Arrott plots are obtained by plotting M^2 against H/M. This curve determined the nature of the phase transition i.e., first order or second order phase transition. According to Banerjee's criterion, the slope of the Arrott plot determines the nature of phase transition. The negative slope corresponds to first order phase transition whereas the positive slope corresponds to second order phase transition [54].

The obtained M vs. H curve at different temperatures is also used to find the change in magnetic entropy at different temperatures. This is a critical parameter for practical application in magnetic refrigeration. Mathematically, the difference in entropy is calculated as follows,

$$-\Delta S(T, \Delta H) = \int_{H_1}^{H_2} \frac{\partial M(T, H)}{\partial T} dH \tag{5}$$

where,

M = magnetization of the sample

H = External applied field

To calculate the magnetic entropy, change from the M vs. H plots, we calculate the area underneath the plot, and the formula is modified as follows,

$$\Delta S(T, \Delta H) = \frac{A_2 - A_1}{T_2 - T_1} \tag{6}$$

Where, A1 and A2 are areas underneath the M vs. H curve at temperatures T1 and T2, respectively.

The change in entropy should be maximum at the phase transition temperature because this quantity is directly proportional to the change in magnetization. The magnetization will

change the most during the transition temperature because, at this point, the magnetic spins align completely towards the direction of the applied magnetic field from a randomized state. The field dependence of this maximum entropy change at any specific temperature is given by the relation

$$\Delta S(H) = CH^N \tag{7}$$

where,

C is a constant and N is the exponent obtained from experimental fitting that determines the sensitivity of magnetic entropy change to the applied field. The higher value of N signifies higher sensitivity of the entropy change to the applied field.

The most crucial parameter in determining the magnetocaloric behavior of a material is Relative Cooling Power (RCP). RCP is the total amount of heat transferred in a complete cycle. It can be calculated using the ΔS_m vs. T plot.

Mathematically,

$$RCP = \Delta S\text{max} \times \delta T_{FWHM} \tag{8}$$

where,

ΔS_{max} = maximum value of entropy changes at the given applied field (peak of ΔS_m vs. T plot)

δT_{FWHM} = Full Width at Half Maxima of the ΔS_m vs. T plot

RCP should increase linearly with the increase in the applied field since the magnetization increases linearly with the applied field, and so does the magnetic entropy change.

The filed dependence of RCP can also be studied using the relation,

$$RCP(H) = DH^R \tag{9}$$

where,

C is a constant and R is the exponent obtained from experimental fitting that determines the sensitivity of RCP to the external applied field.

Furthermore, the specific heat of the material is calculated using the ΔS_m vs. T plot. Specific heat is the amount of energy required to change the temperature of a unit mass of a substance by 1 K. So, low values of specific heat imply that less energy is required to change the temperature for the same mass of the material. Thus, low specific heat is a better condition for a refrigerant.

Mathematically, specific heat is calculated as,

$$C_p(T, \Delta H) = T \frac{\partial S}{\partial T} \tag{10}$$

To calculate specific heat using the data values, we modify the formula as follows,

$$C_p(T, \Delta H) = T \frac{S_2 - S_1}{T_2 - T_1} \tag{11}$$

where,

S_1 and S_2 are entropies at temperatures T_1 and T_2, respectively.

Chapter 5 Results and Discussion

5.1 Synthesis

In this work, we have synthesized $(1\text{-}x)$ $La_{0.7}Ca_{0.3}MnO_3\text{-}x$MO ($x = 0.0\%, 2.5\%, 5\%$; M = Ni, Cu, Co) composites using a simple autocombustion method. We have used $La(NO_3)_3.6H_2O$, $Ca(NO_3)_2.4H_2O$, and $Mn(NO_3)_2.4H_2O$ as precursors for the preparation of $La_{0.7}Ca_{0.3}MnO_3$ perovskite with Citric Acid as the fuel. Similarly, $Ni(NO_3)_2.6H_2O$, $Cu(NO_3)_2.3H_2O$ and $Co(NO_3)_2.6H_2O$ were used as precursors for respective metal oxide formation with Citric Acid as fuel. All of the used chemicals were obtained from Sigma Aldrich with >99% purity.

The synthesis process is demonstrated in the schematic given below.

Fig. 5.1. Schematic of preparation of $La_{0.7}Ca_{0.3}MnO_3$-x%MO ($x = 0.0\%, 2.5\%, 5.0\%$) (M = Ni, Cu, Co) using autocombustion method.

The stoichiometric amounts of $La(NO_3)_3.6H_2O$, $Ca(NO_3)_2.4H_2O$, $Mn(NO_3)_2.4H_2O$, and citric acid as given in Table 5.1 were dissolved in 25 ml De-ionized (DI) water and ultrasonicated for one hour to form a homogeneous solution. The pH of this solution was maintained at 10 to ensure the desired nanosized synthesis of the perovskite. At the same time, the stoichiometric amounts of respective metal nitrate precursor and citric acid, given in Table 5.2 was also dissolved in 15 ml DI water and ultrasonicated for one hour to form a homogeneous solution of respective metal nitrates.

Table 5.1. Stoichiometry of chemicals used for the synthesis of $La_{0.7}Ca_{0.3}MnO_3$.

Sample	Mass (grams)			
	$La(NO_3)_3.6H_2O$	$Ca(NO_3)_2.4H_2O$	$Mn(NO_3)_2.4H_2O$	Citric Acid
$La_{0.7}Ca_{0.3}MnO_3$	1.4284	0.3338	1.1829	2.9709
$La_{0.7}Ca_{0.3}MnO_3$-2.5%NiO	1.3927	0.3255	1.1533	2.8967
$La_{0.7}Ca_{0.3}MnO_3$-5%NiO	1.3570	0.3171	1.1237	2.8224
$La_{0.7}Ca_{0.3}MnO_3$-2.5%CuO	1.3927	0.3255	1.1533	2.8967
$La_{0.7}Ca_{0.3}MnO_3$-5%CuO	1.3570	0.3171	1.1237	2.8224
$La_{0.7}Ca_{0.3}MnO_3$-2.5%CoO	1.3927	0.3255	1.1533	2.8967
$La_{0.7}Ca_{0.3}MnO_3$-5%CoO	1.3570	0.3171	1.1237	2.8224

Table 5.2. Stoichiometry of chemicals used for the synthesis of metal oxides (NiO, CuO, CoO).

Sample	Mass (grams)			
	$Ni(NO_3)_2.6H_2O$	$Cu(NO_3)_2.3H_2O$	$Co(NO_3)_2.6H_2O$	Citric Acid
$La_{0.7}Ca_{0.3}MnO_3$-2.5%NiO	0.0973	N/A	N/A	0.0703
$La_{0.7}Ca_{0.3}MnO_3$-5%NiO	0.1946	N/A	N/A	0.1406
$La_{0.7}Ca_{0.3}MnO_3$-2.5%CuO	N/A	0.0731	N/A	0.0660
$La_{0.7}Ca_{0.3}MnO_3$-5%CuO	N/A	0.1462	N/A	0.1320
$La_{0.7}Ca_{0.3}MnO_3$-2.5%CoO	N/A	N/A	0.0970	0.0701
$La_{0.7}Ca_{0.3}MnO_3$-5%CoO	N/A	N/A	0.1941	0.1402

These two solutions were mixed and again ultrasonicated for one hour. The obtained solution was heated on a hot plate at 80°C for gelation. After a gel-like substance was observed, the temperature was increased to 300°C for the auto combustion. After the gel-like substance hardened into a fluffy solid phase, the product was ground to a fine powder. The ground particles were finally calcined at 1100°C to obtain the desired nano composites. The reaction occurring is as follows,

$$La(NO_3)_3.6H_2O + Ca(NO_3)_2.4H_2O + Mn(NO_3)_2.4H_2O + C_6H_8O_7.H_2O$$

$$\downarrow$$

$$La_{0.7}Ca_{0.3}MnO_3 + H_2O + N_2\uparrow + CO_2\uparrow$$

Also,

$$M(NO_3).xH_2O + C_6H_8O_7.H_2O \longrightarrow MO + H_2O + N_2\uparrow + CO_2\uparrow$$
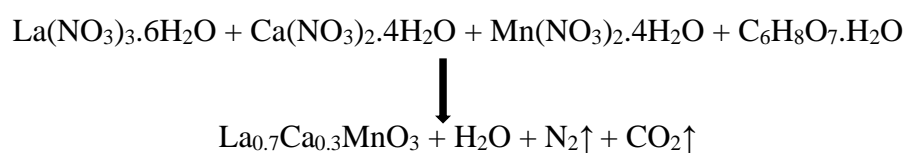
where, M = Ni, Cu, Co

5.2 Structural Characterization

The prepared samples were studied using various techniques for structural and magnetocaloric properties. Structural and phase determination of sample was performed using X-ray diffraction (XRD), while morphological and chemical study done via scanning electron microscopy (SEM) and energy dispersive spectroscopy (EDS).

5.2.1 X-ray diffraction (XRD)

X-ray diffraction is helpful to determine the purity structure and different structural parameters of the sample. Fig. 5.2 shows that all our samples are pure and the presence of respective metal oxide phases. There are no extra secondary phases present in the sample. Since the metal oxide is only present in a small amount as compared to the perovskite $La_{0.7}Ca_{0.3}MnO_3$, the perovskite phase is very dominant compared to the metal oxide phase. It is hard to observe the metal oxide phase on the same scale as the perovskite phase.

This XRD spectrum is refined using TOPAS software to determine the lattice parameters and cell volume of the composite samples which are given in Table 5.3Table 5.3. Lattice parameters and cell volume of $La_{0.7}Ca_{0.3}MnO_3$ and MO phase in $La_{0.7}Ca_{0.3}MnO_3$-x%MO (x = 0.0%, 2.5%, 5.0%) composite system.. The minimal to no change in the lattice parameter value suggests that there is possibly no inclusion of additional elements to the perovskite structure. This suggests that the metal oxides are present as composites to the perovskites in the grain boundaries.
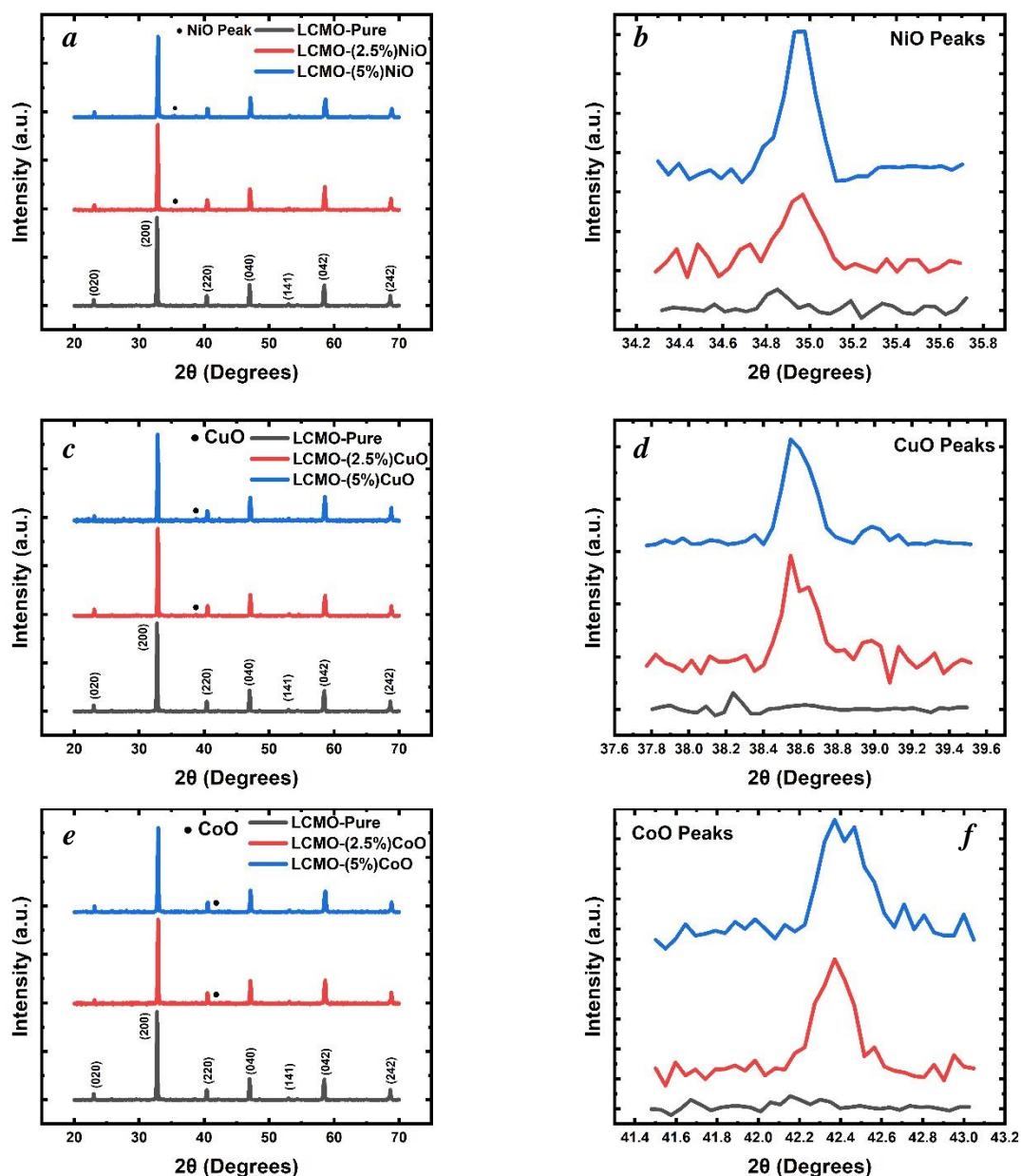
Fig. 5.2. XRD spectrum of a) La₀.₇Ca₀.₃MnO₃-x%NiO (x = 0.0%, 2.5%, 5.0%), b) long run NiO peaks, c) La₀.₇Ca₀.₃MnO₃-x%CuO (x = 0.0%, 2.5%, 5.0%), d) long run CuO peaks, e) La₀.₇Ca₀.₃MnO₃-x%CoO (x = 0.0%, 2.5%, 5.0%), and f) long run CoO peaks.

The analysis of the spectra also showed that the $La_{0.7}Ca_{0.3}MnO_3$ perovskite exists in the

orthorhombic phase (space group: Pnma, ICDD no.: 00-063-0088). The metal oxides NiO

(ICDD no.: 01-085-5454) and CoO (ICDD no.: 01-071-1178) exist in a cubic phase (space

group: Fm-3m), whereas CuO (ICDD no.: 01-086-8837) exists in the monoclinic phase
(space group: C12/c1).

Table 5.3. Lattice parameters and cell volume of La$_{0.7}$Ca$_{0.3}$MnO$_3$ and MO phase in La$_{0.7}$Ca$_{0.3}$MnO$_3$-x%MO (x = 0.0%, 2.5%, 5.0%) composite system.

Sample	La$_{0.7}$Ca$_{0.3}$MnO$_3$ Phase				Metal Oxide Phase			
	a(Å) (±0.01)	b(Å) (±0.01)	c(Å) (±0.01)	Cell Volume(Å^3) (±0.1)	a(Å) (±0.01)	b(Å) (±0.01)	c(Å) (±0.01)	Cell Volume(Å^3) (±0.1)
LCMO Pure	5.460	7.712	5.469	230.489		NA		NA
LCMO-(2.5%)NiO	5.465	7.713	5.459	230.133	3.789	NA	NA	54.423
LCMO-(5%)NiO	5.456	7.698	5.448	228.862	4.293	NA	NA	79.098
LCMO-(2.5%)CuO	5.458	7.689	5.444	228.498	4.693	3.317	5.129	79.839
LCMO-(5%)CuO	5.467	7.702	5.456	229.727	4.783	3.369	5.156	83.051
LCMO-(2.5%)CoO	5.409	7.680	5.438	225.957	4.319	NA	NA	80.574
LCMO-(5%)CoO	5.452	7.712	5.440	228.738	4.313	NA	NA	80.253

Further, the crystallite size of the samples was calculated using Scherrer's method. According to Scherrer's method, grain size is given by equation (2). The diffraction peaks with miller indices (hkl) values (020), (200), (220), (040), (042) and (242) corresponding to peak positions (2θ) 23.1º, 32.8º, 40.4º, 47.1º, 58.5º and 68.7º were used to calculate the crystallite size. The obtained crystallite size is given in Table 5.4. The crystallite size has shown consistent decrease with the increasing content of metal oxides.

Table 5.4. Crystallite size of La$_{0.7}$Ca$_{0.3}$MnO$_3$-x%MO (x = 0.0%, 2.5%, 5.0%) composite system obtained using Scherrer's method.

Sample	*Crystallite Size(nm)*
La$_{0.7}$Ca$_{0.3}$MnO$_3$	*48.85 ($\pm$4.41)*
La$_{0.7}$Ca$_{0.3}$MnO$_3$-2.5%NiO	*48.01 ($\pm$4.59)*
La$_{0.7}$Ca$_{0.3}$MnO$_3$-5%NiO	*42.37 ($\pm$3.92)*
La$_{0.7}$Ca$_{0.3}$MnO$_3$-2.5%CuO	*47.70 ($\pm$4.39)*
La$_{0.7}$Ca$_{0.3}$MnO$_3$-5%CuO	*47.15 ($\pm$4.66)*
La$_{0.7}$Ca$_{0.3}$MnO$_3$-2.5%CoO	*46.83 ($\pm$4.19)*
La$_{0.7}$Ca$_{0.3}$MnO$_3$-5%CoO	*43.06 ($\pm$3.93)*

HWL plot is also used to determine the crystalline size and strain in the sample. The same peaks used for Scherrer's method i.e., (020), (200), (220), (040), (042) and (242) corresponding to peak positions (2θ) 23.1º, 32.8º, 40.4º, 47.1º, 58.5º and 68.7º were used. Fig. 5.3 represents the HWL plots for all the samples with respective linear fits.

Fig. 5.3 was used to determine the crystallite size and the lattice strain using the slope and the intercept which are documented in Table 5.5. We can see the reduction of crystallite size as the content of metal oxide in the composite increases. This is attributed to the deposition of metal oxides in the grain boundaries which would restrict the agglomeration of La$_{0.7}$Ca$_{0.3}$MnO$_3$ and hence reducing the crystallite size [55,56].
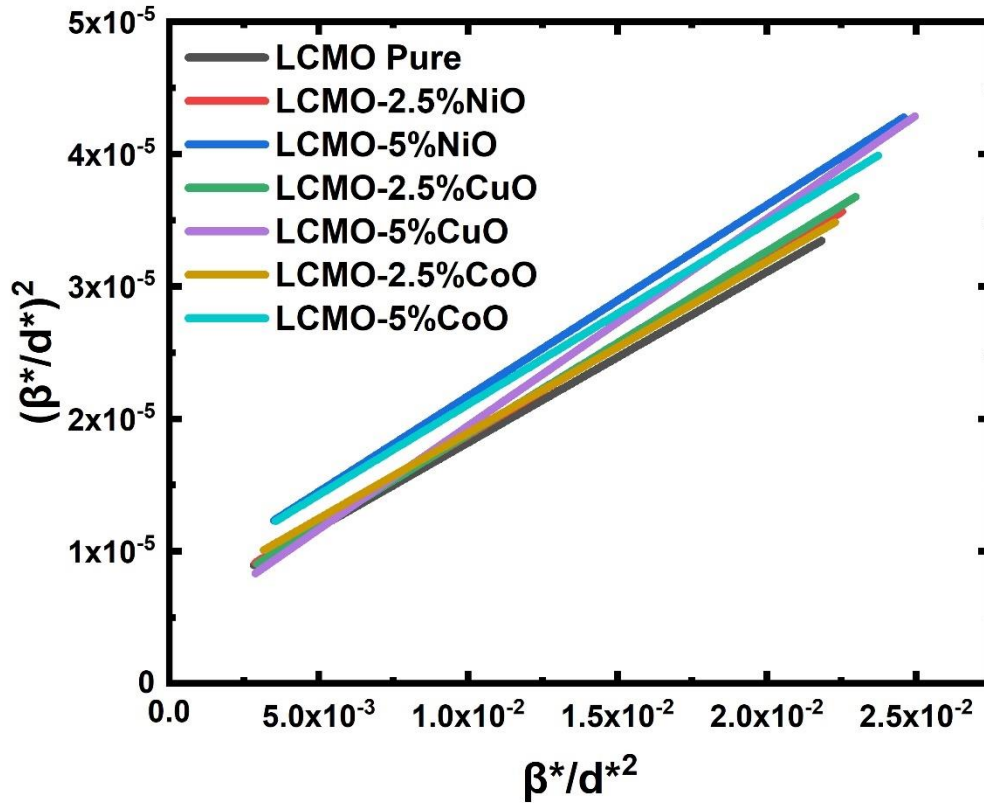
Fig. 5.3. Linear fits for HWL plots of La$_{0.7}$Ca$_{0.3}$MnO$_3$-x%MO (x = 0.0%, 2.5%, 5.0%).

Table 5.5. Crystallite size and lattice strain of La$_{0.7}$Ca$_{0.3}$MnO$_3$-x%MO (x = 0.0%, 2.5%, 5.0%) composite system obtained using HWL Method.

Sample	Crystallite Size(nm)	Strain (x10^{-6})
La$_{0.7}$Ca$_{0.3}$MnO$_3$	77.52 (±14.03)	5.308 (±2.76)
La$_{0.7}$Ca$_{0.3}$MnO$_3$-2.5%NiO	74.07 (±14.57)	5.256 (±3.21)
La$_{0.7}$Ca$_{0.3}$MnO$_3$-5%NiO	69.44 (±14.73)	7.270 (±4.07)
La$_{0.7}$Ca$_{0.3}$MnO$_3$-2.5%CuO	72.46 (±13.07)	4.979 (±3.03)
La$_{0.7}$Ca$_{0.3}$MnO$_3$-5%CuO	64.10 (±10.30)	3.828 (±3.21)
La$_{0.7}$Ca$_{0.3}$MnO$_3$-2.5%CoO	76.92 (±14.69)	5.982 (±3.00)
La$_{0.7}$Ca$_{0.3}$MnO$_3$-5%CoO	72.99 (±15.46)	7.411 (±3.76)

5.2.2 Scanning Electron Microscopy (SEM) and Energy Dispersive Spectroscopy (EDS)

Scanning electron microscopy (SEM) was performed on all the samples to understand the morphology and structure of the composite system. Fig. 5.4, Fig. 5.5, Fig. 5.6, and Fig. 5.7 show the SEM images, EDS mapping, and EDS spectra with weight proportions of $La_{0.7}Ca_{0.3}MnO_3$, $La_{0.7}Ca_{0.3}MnO_3$-5%NiO, $La_{0.7}Ca_{0.3}MnO_3$-5%CuO and $La_{0.7}Ca_{0.3}MnO_3$-5%CoO samples, respectively. .

Table 5.6 gives the atomic percentages of all elements present in the respective samples.

 The morphology and the structure of the samples seem unchanged with the addition of metal oxide phases which confirms that there is no reaction between LCMO and metal oxides. Also, the presence of metal elements in the respective composites is confirmed by the EDS mapping. Moreover, the composites' oxygen weight and atomic percentage have increased, which suggests that the metal elements are present as oxides in the samples. This further confirms the formation of composites and the absence of reaction between LCMO and metal oxides.
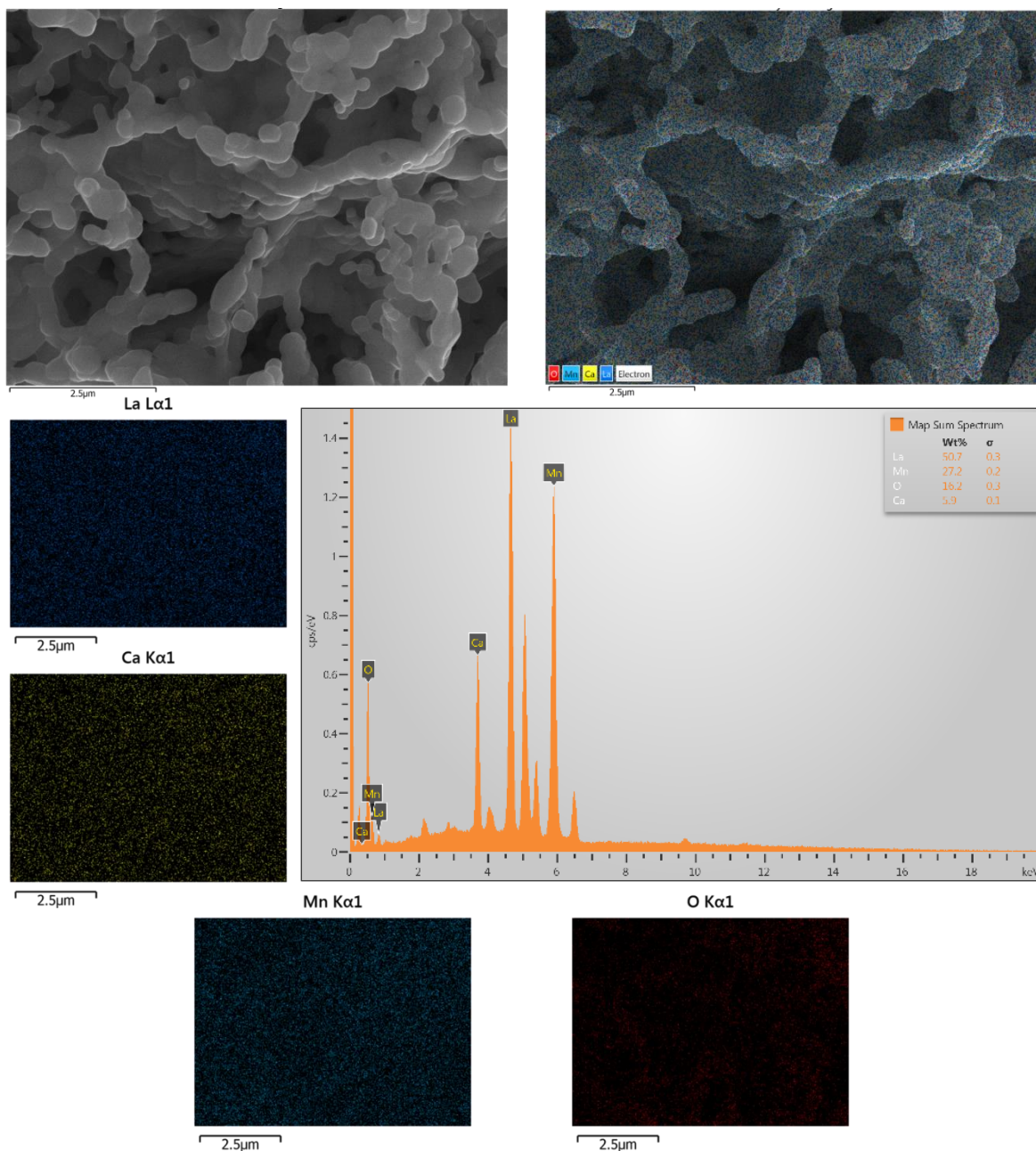
Fig. 5.4. From top left: SEM image, EDS mapping traces, and EDS spectrum with weight ratios of available elements on La₀.₇Ca₀.₃MnO₃.
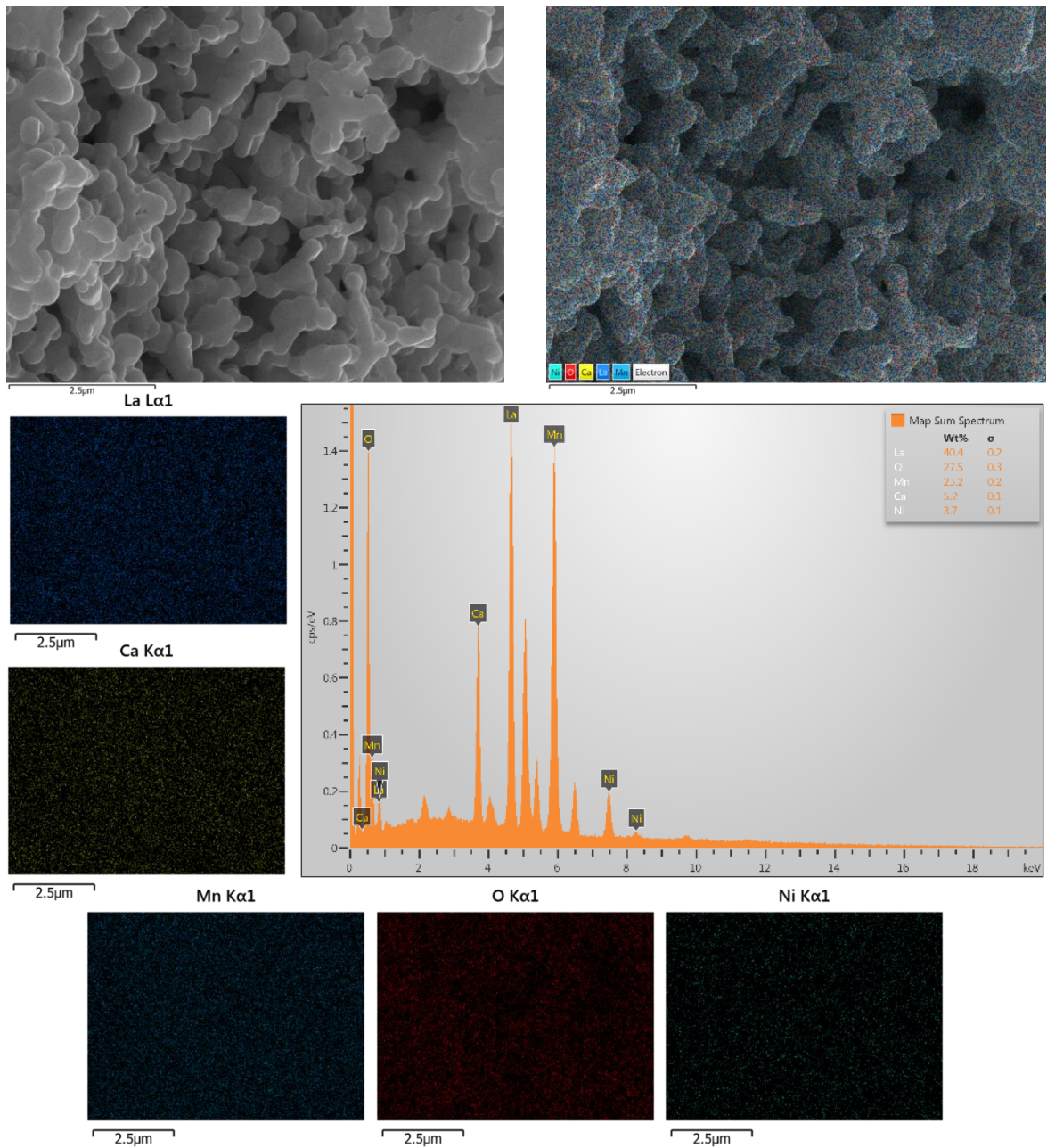
Fig. 5.5. From top left: SEM image, EDS mapping traces, and EDS spectrum with weight ratios of available elements on La₀.₇Ca₀.₃MnO₃-5%NiO.
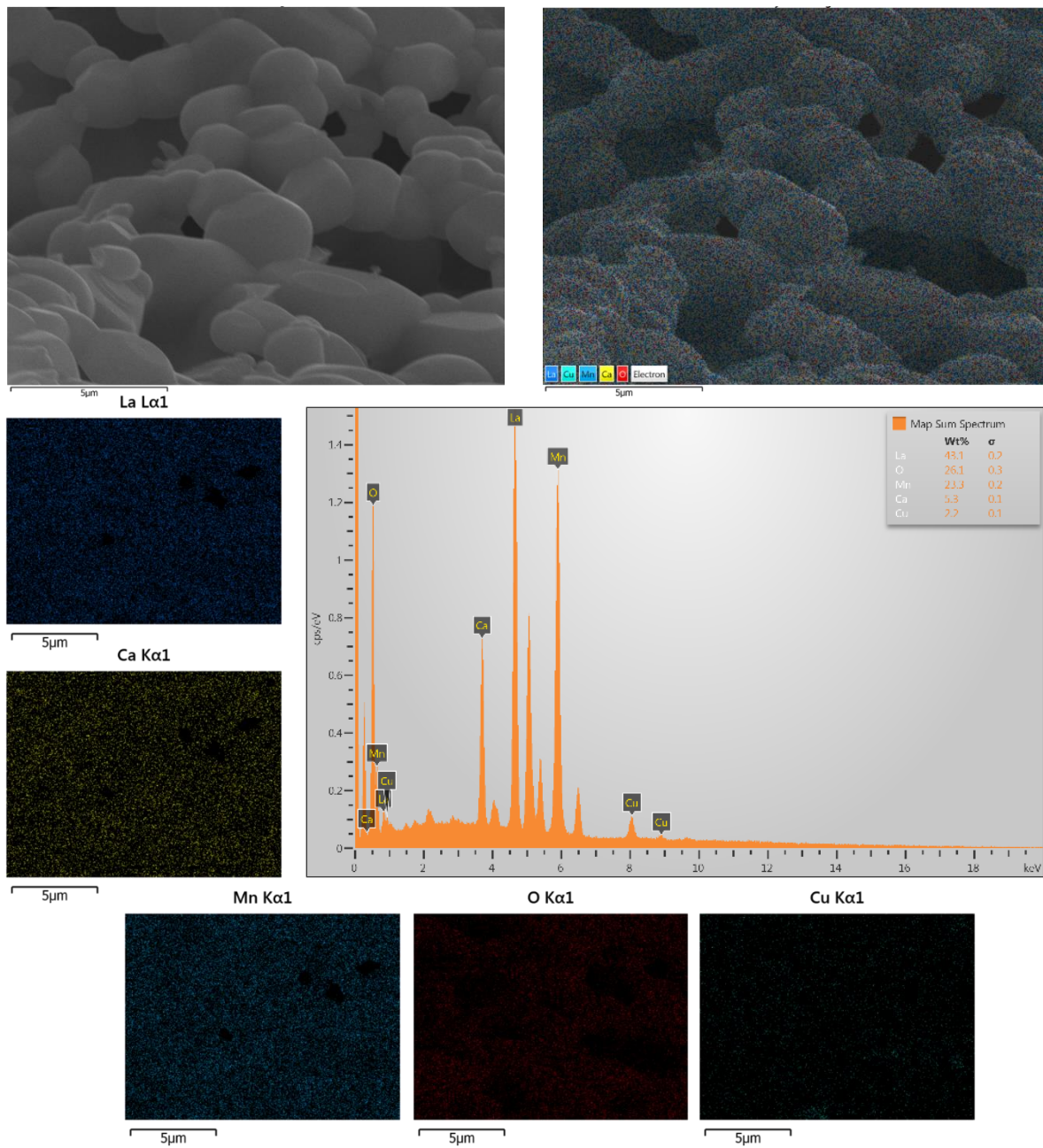
Fig. 5.6. From top left: SEM image, EDS mapping traces, and EDS spectrum with weight ratios of available elements on La$_{0.7}$Ca$_{0.3}$MnO$_3$-5%CuO.
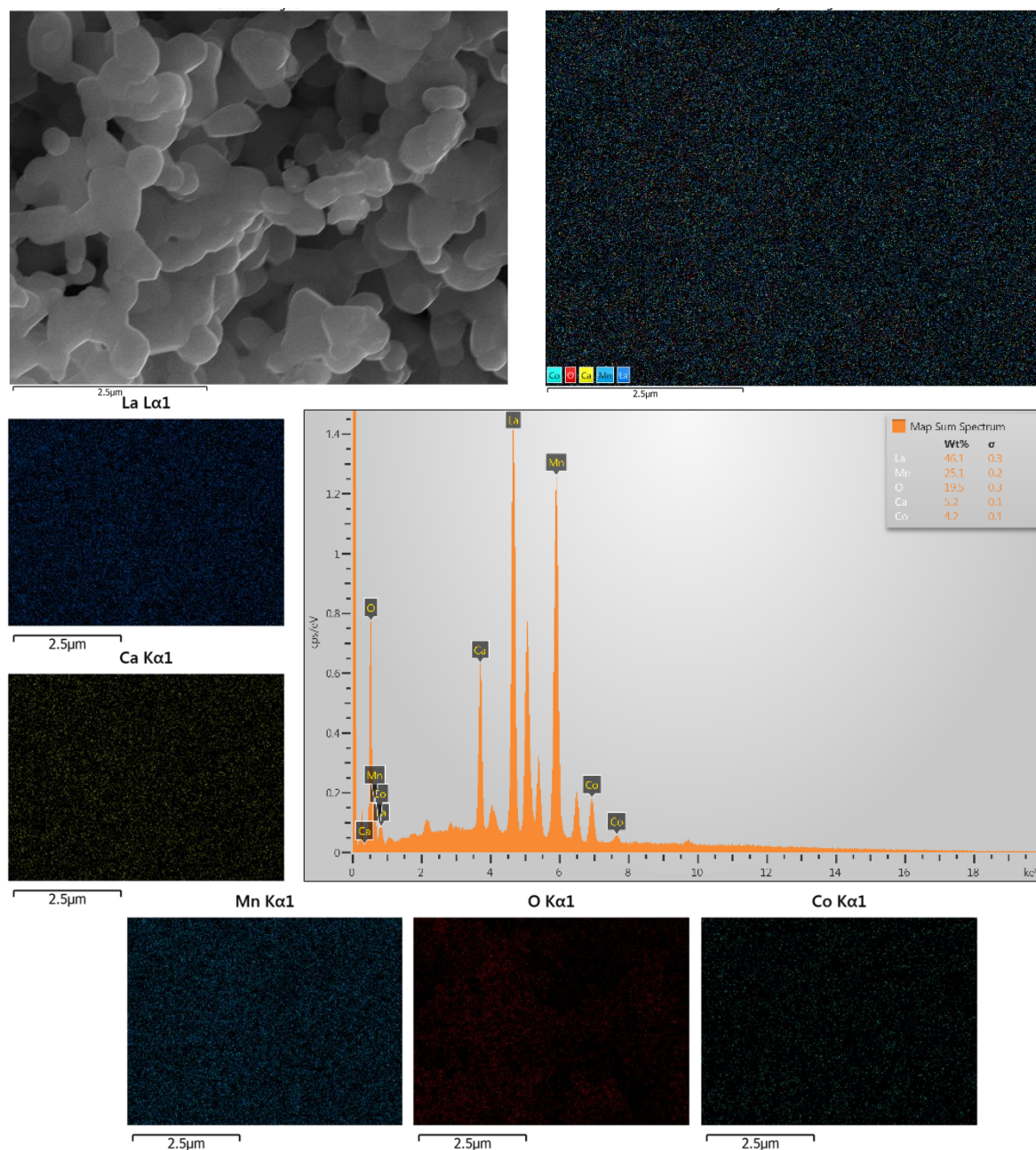
Fig. 5.7. From top left: SEM image, EDS mapping traces, and EDS spectrum with weight ratios of available elements on La$_{0.7}$Ca$_{0.3}$MnO$_3$-5%CoO.

Table 5.6. The atomic percentage obtained for different samples from EDS.

Element	Atomic %			
	LCMO	*LCMO-5%NiO*	*LCMO-5%CuO*	*LCMO-5%CoO*
La	*18.09*	*11.06*	*12.26*	*15.05*
Ca	*7.31*	*4.96*	*5.23*	*5.89*
Mn	*24.52*	*16.06*	*16.74*	*20.68*
O	*50.09*	*65.52*	*64.40*	*55.17*
Ni/Cu/Co	*N/A*	*2.40*	*1.37*	*3.20*

5.2.3 Magnetocaloric Study

The Quantum Design Physical Property Measurement System (PPMS) DynaCool (The Buffalo State University of New York) was used to measure different magnetic parameters at varying temperatures to understand the magnetocaloric properties of the samples.

The magnetization of the samples was measured with a decrease in temperature at a constant external applied field of 1 kOe (0.1 T). This is the field Cooled (FC) curve shown in Fig. 5.8. We can see that the sample undergoes a phase transition from its paramagnetic phase to a ferromagnetic phase when the temperature is decreased. This is exhibited by the immediate increase in the magnetization of the sample at a specific temperature point, which is called the phase transition temperature (Tc). We notice that the temperature of the transition decreases with the increasing content of metal oxide in the composite. Also, the curve becomes broader, and the sharpness of the fall also decreases with the increase in the amount of metal oxides.

The saturation magnetization of the sample in the ferromagnetic state at lower temperature seems to remain close for the 2.5% sample in LCMO-NiO and LCMO-CuO. The saturation magnetization has dropped for all other samples compared to that of the pristine LCMO. This drop-in magnetization is due to the introduction of antiferromagnetic metal oxides phases in the ferromagnetic perovskite structure. This mixture of different magnetic phases induces magnetic inhomogeneity, which causes the loss of net ferromagnetic ordering and hence the magnetization drops.
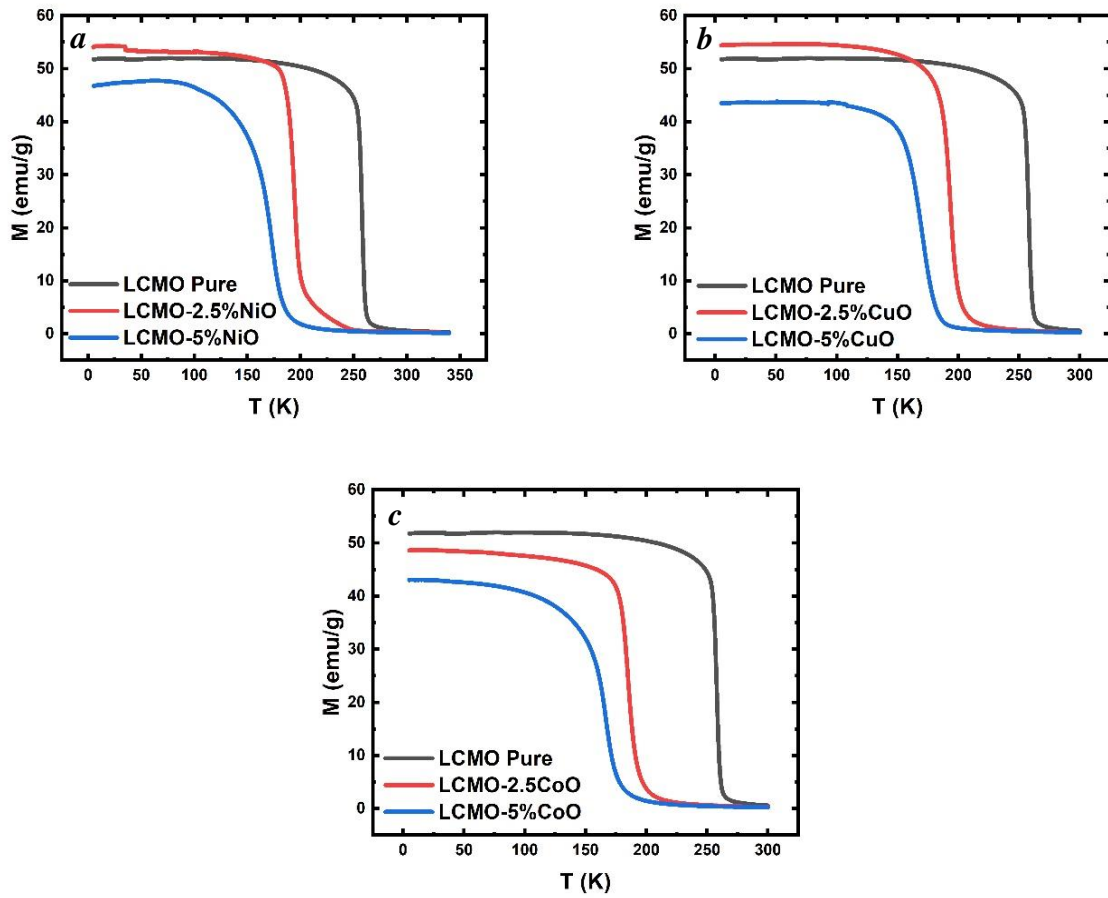
Fig. 5.8. Field Cooled (FC) curve of a) La_{0.7}Ca_{0.3}MnO₃-x%NiO (x = 0.0%, 2.5%, 5.0%), b) ***La₀.₇Ca₀.₃MnO₃-x%CuO (x = 0.0%, 2.5%, 5.0%), and c) La₀.₇Ca₀.₃MnO₃-x%CoO (x =*** ***0.0%, 2.5%, 5.0%) at an external applied field of 1kOe.***

The effect of composite formation on the paramagnetic to ferromagnetic (PM-FM) transition

temperature can be better understood by differentiating the FC curve. The obtained plots,

dM/dT vs. T are shown in Fig. 5.9. The peak of this curve represents the phase transition

temperature, and the broadness of the peak suggests if the transition is immediate or over a

wide range of temperatures.
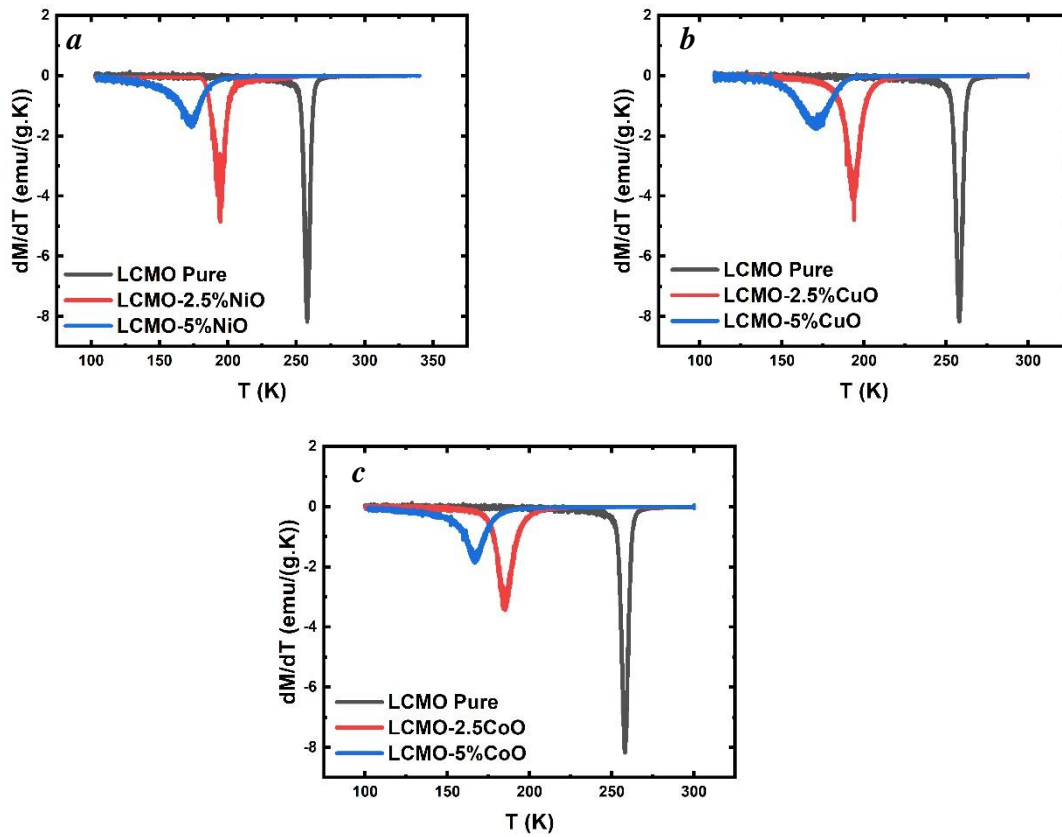
Fig. 5.9. dM/dT vs T plot of a) $La_{0.7}Ca_{0.3}MnO_3$-x%NiO (x = 0.0%, 2.5%, 5.0%), b) $La_{0.7}Ca_{0.3}MnO_3$-x%CuO (x = 0.0%, 2.5%, 5.0%), and c) $La_{0.7}Ca_{0.3}MnO_3$-x%CoO (x = 0.0%, 2.5%, 5.0%).

The phase transition temperatures have been evaluated from Fig. 5.9 and recorded in Table 5.7. The transition temperature of 258 K for pure LCMO is in close agreement with 267 K recorded in literature [22]. The transition temperature has dropped on all composites with increasing content of metal oxides. The drop in transition temperature is very similar for LCMO-NiO, and LCMO CuO samples, but a slightly higher drop is observed in LCMO-CoO samples. The temperature drops from 258 K for pristine LCMO to 166.6 K in LCMO-5%CoO sample is the most significant observed. Also, the peaks broaden as the content of metal oxide increases. The intensity of the rate of change of magnetization with respect to temperature decreases with respect to an increase in metal oxide content. This implies that the

41

phase transition ranges over a more extensive range of temperature as compared to the

pristine LCMO.

Table 5.7. Magnetic phase transition temperature of $La_{0.7}Ca_{0.3}MnO_3$-x%MO (x = 0.0%, 2.5%, 5.0%) composites.

Sample	Phase Transition Temperature (T_c)
$La_{0.7}Ca_{0.3}MnO_3$	258.0 K
$La_{0.7}Ca_{0.3}MnO_3$-2.5%NiO	194.6 K
$La_{0.7}Ca_{0.3}MnO_3$-5%NiO	173.3 K
$La_{0.7}Ca_{0.3}MnO_3$-2.5%CuO	193.9 K
$La_{0.7}Ca_{0.3}MnO_3$-5%CuO	171.7 K
$La_{0.7}Ca_{0.3}MnO_3$-2.5%CoO	185.2 K
$La_{0.7}Ca_{0.3}MnO_3$-5%CoO	166.6 K

This drop-in phase transition temperature is due to the magnetic insulation of

antiferromagnetic metal oxide composites [41, 43]. The antiferromagnetic metal oxides

present in the grain boundaries of the LCMO cause the loss of ordering of the magnetic spins

of the perovskite resulting in the decrease of the phase transition temperature and broadening

of the peak.

Furthermore, isothermal curves were obtained by measuring the sample's magnetization with

varying external magnetic fields at different temperatures around the respective phase

transition temperature. The measurements were taken at an interval of 4-5K to obtain more

accurate data. Figures represent the M vs. H plot at different temperature values for all the

samples. The obtained curves are presented in Fig. 5.10.
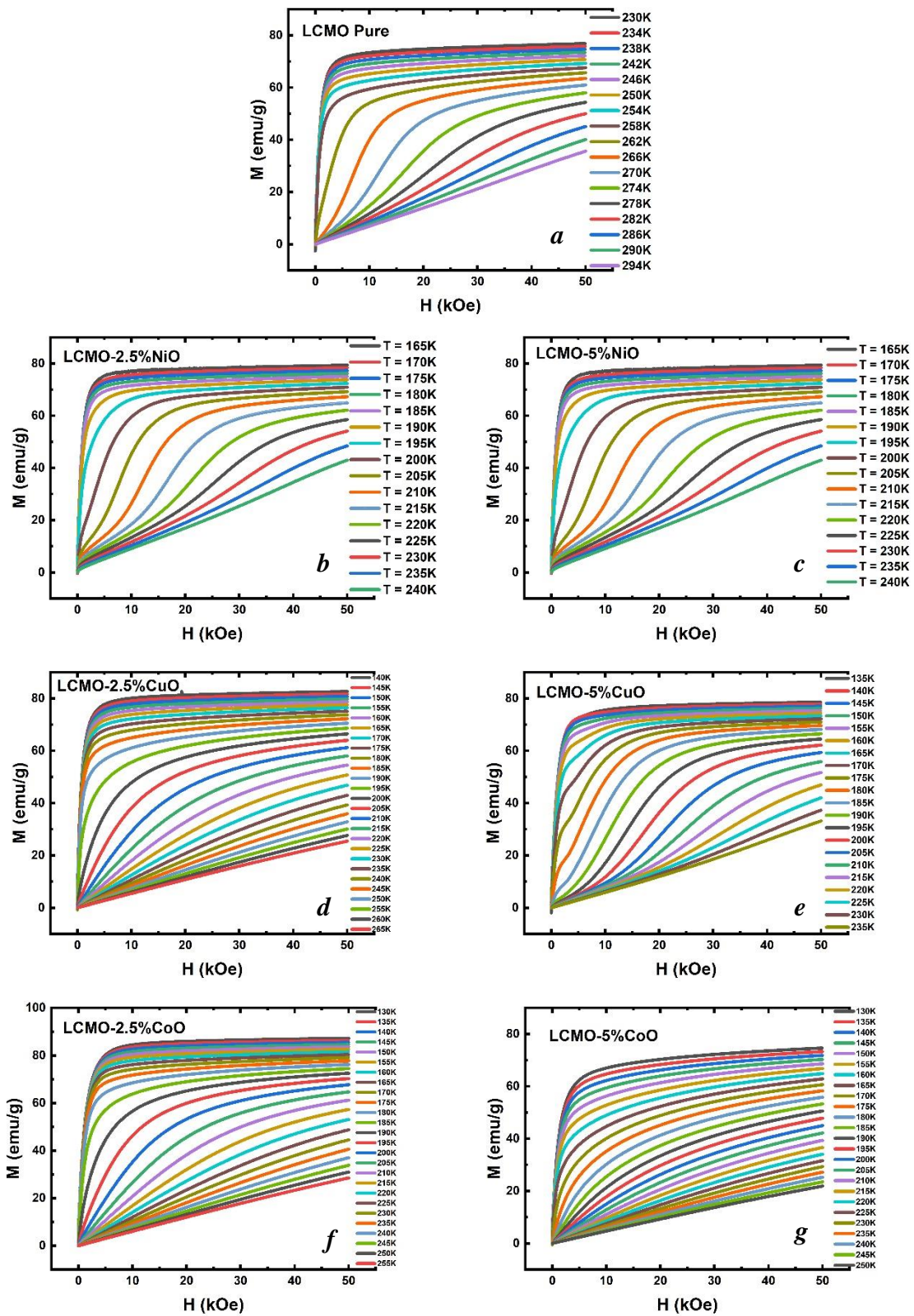
Fig. 5.10. M vs H curves of a) La₀.₇Ca₀.₃MnO₃, b) La₀.₇Ca₀.₃MnO₃-2.5%NiO, c) *La$_{0.7}$Ca$_{0.3}$MnO$_3$-5%NiO, d) La$_{0.7}$Ca$_{0.3}$MnO$_3$-2.5%CuO, e) La$_{0.7}$Ca$_{0.3}$MnO$_3$-5%CuO, f) La$_{0.7}$Ca$_{0.3}$MnO$_3$-2.5%CoO, and g) La$_{0.7}$Ca$_{0.3}$MnO$_3$-5%CoO at different temperatures.*

From Fig. 5.10 also, we can see that the samples undergo a phase transition from paramagnetic to ferromagnetic phase as we move from higher to lower temperatures. The bottom part of the graph represents the higher temperature measurements and decreases gradually with an interval of 4-5K as we go up. The plot at a higher value of temperatures is straight lines passing through the origin, representing the paramagnetic phase. As we go to lower temperatures, we can see that the graph changes nature and acquires more of a ferromagnetic ordering with the magnetization saturation in the presence of the external magnetic field. We notice the jump of magnetization values for the same external field with a temperature decrease. The highest jump of magnetization corresponds to the phase transition temperature. This is because the magnetization shows a sharp increase at that point of transition from paramagnetic to ferromagnetic phase.

Fig. 5.11 represents the Arrott plots for all the samples. According to Banerjee, the slope of this curve determines the nature of magnetic phase transition [54]. The negative slope corresponds to first order phase transition whereas the positive slope corresponds to the second order phase transition. We have observed a first order phase transition in $La_{0.7}Ca_{0.3}MnO_3$, $La_{0.7}Ca_{0.3}MnO_3$-2.5%NiO, and $La_{0.7}Ca_{0.3}MnO_3$-5%CuO whereas a second order phase transition in $La_{0.7}Ca_{0.3}MnO_3$-5%NiO, $La_{0.7}Ca_{0.3}MnO_3$-2.5%CuO, $La_{0.7}Ca_{0.3}MnO_3$-2.5%CoO, and $La_{0.7}Ca_{0.3}MnO_3$-5%CoO. The change of order of magnetic phase transition can be attributed to the particle size reduction [57]. The formation of composites causes the reduction of crystallite size as explained earlier which causes the shift of magnetic phase transition from first order to second order.
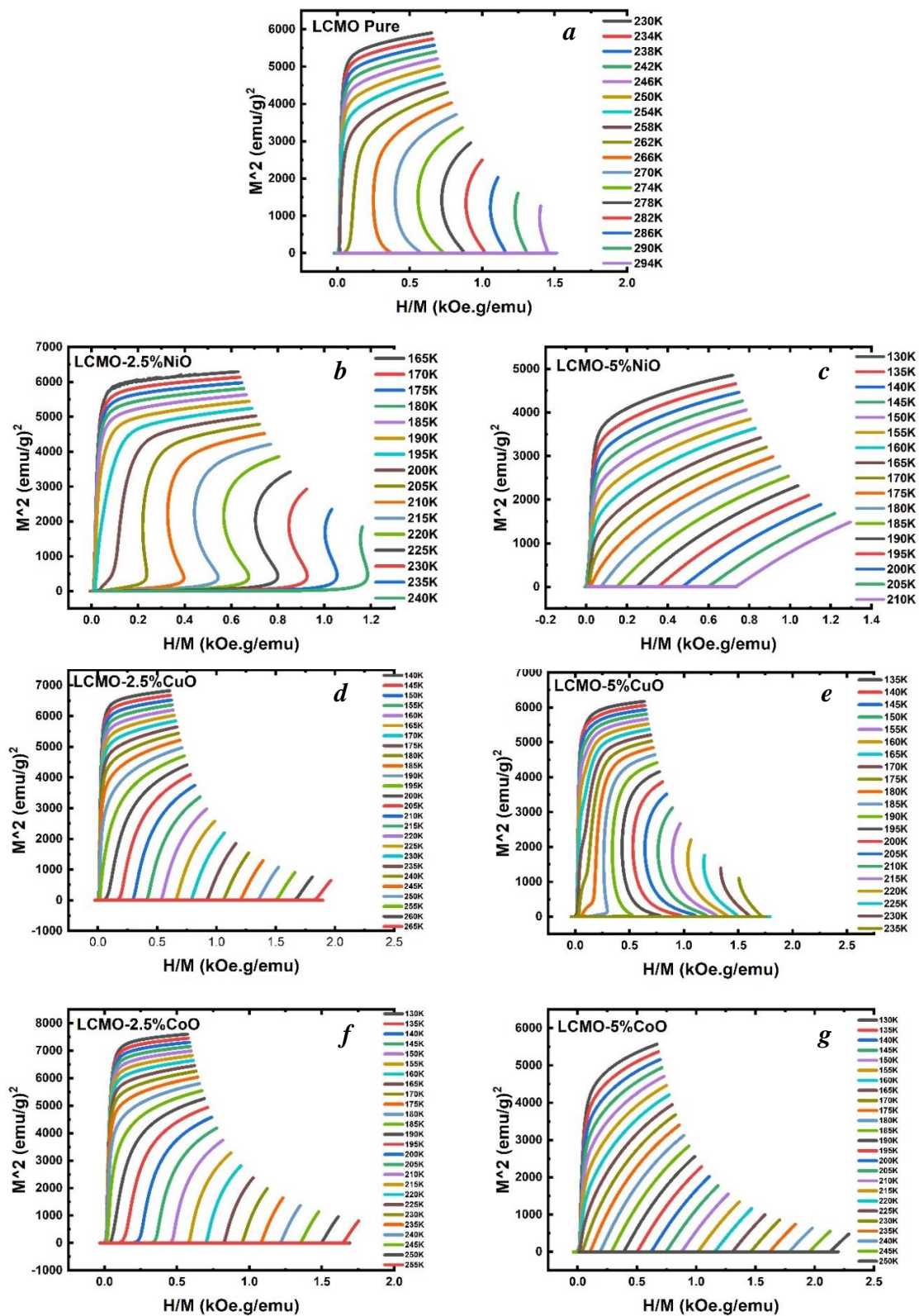
Fig. 5.11. Arrott plots for a) La₀.₇Ca₀.₃MnO₃, b) La₀.₇Ca₀.₃MnO₃-2.5%NiO, c) La₀.₇Ca₀.₃MnO₃-5%NiO, d) La₀.₇Ca₀.₃MnO₃-2.5%CuO, e) La₀.₇Ca₀.₃MnO₃-5%CuO, f) La₀.₇Ca₀.₃MnO₃-2.5%CoO, and g) La₀.₇Ca₀.₃MnO₃-5%CoO.

From M vs. H curves at different temperatures, we can evaluate the change in magnetic entropy of the sample. This is one of the important parameters to quantify the magnetocaloric property of the sample. The change in magnetic entropy is calculated using equation (5).

We plot this negative change in entropy with the temperature at different values of the external field applied. The change in entropy is negative because heat is released during this process. In other words, for an adiabatic process, we can observe a cooling effect during this phenomenon. We can see that this change in entropy is maximum at the phase transition temperature and increases with the increase in the external field applied. Fig. 5.12 represents the negative change in magnetic entropy plotted against temperature at different applied fields from 1 to 5 T.
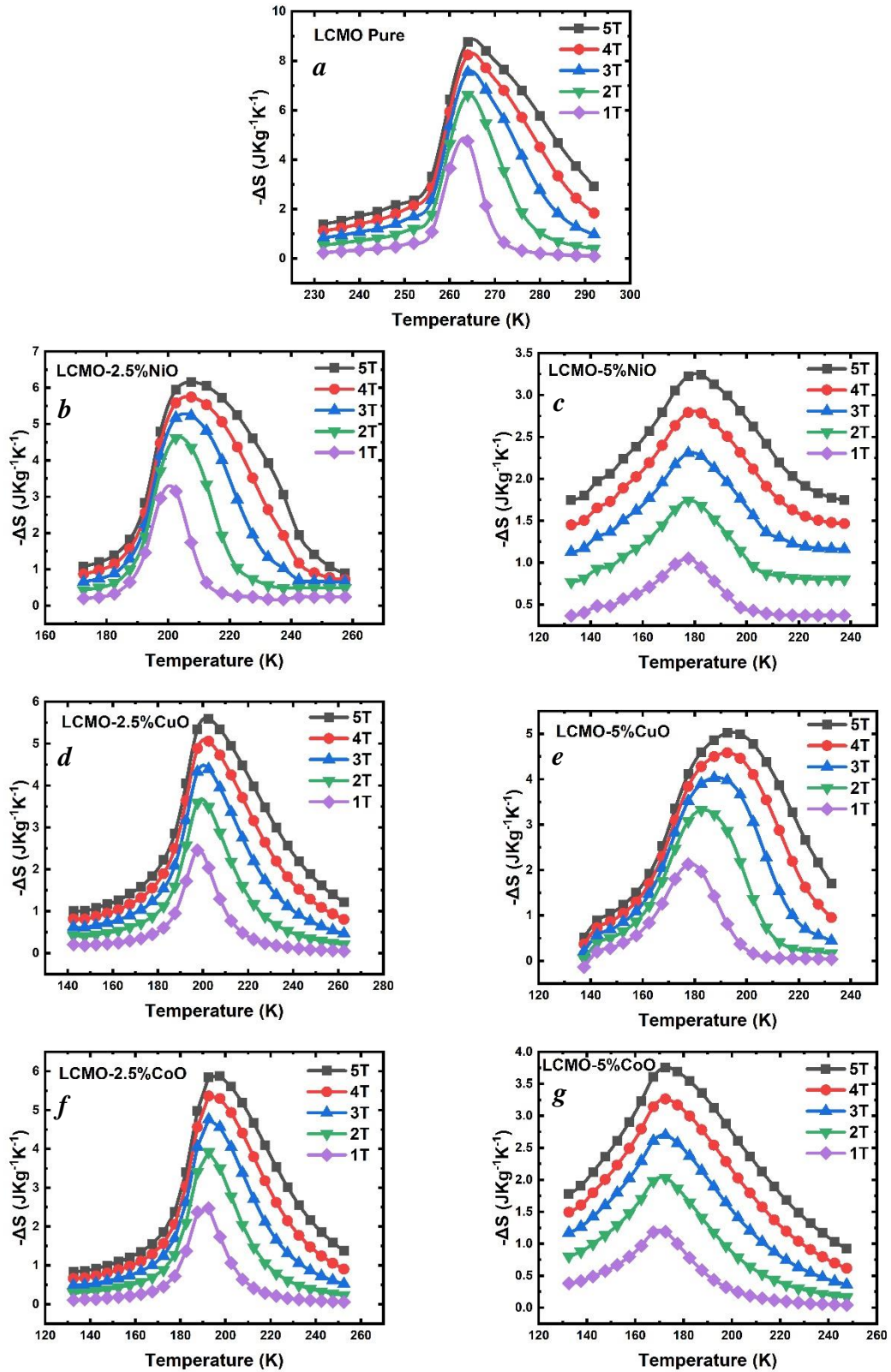
Fig. 5.12. Magnetic entropy change of a) La₀.₇Ca₀.₃MnO₃, b) La₀.₇Ca₀.₃MnO₃-2.5%NiO, c) La₀.₇Ca₀.₃MnO₃-5%NiO, d) La₀.₇Ca₀.₃MnO₃-2.5%CuO, e) La₀.₇Ca₀.₃MnO₃-5%CuO, f) La₀.₇Ca₀.₃MnO₃-2.5%CoO, and g) La₀.₇Ca₀.₃MnO₃-5%CoO at different applied fields.

The maximum change in magnetic entropy and the FWHM of the plot are evaluated from the graph and presented in Table 5.8, Table 5.9, and Table 5.10 for LCMO-NiO, LCMO-CuO, and LCMO-CoO samples, respectively. We can see that the magnetic entropy increases with the increase in strength of the applied field. The magnetic entropy change is maximum at 5T for all the samples, which is because the large applied magnetic field induces higher ferromagnetic ordering. First, the maximum magnetic entropy change obtained for pristine LCMO is 4.75 $JKg^{-1}K^{-1}$ at 1 T, significantly higher than the recorded value of 1.2 $JKg^{-1}K^{-1}$ at 1.5 T [22]. We can see a consistent decrease in the maximum magnetic entropy and peak broadening as the content of metal oxide increases in the sample. The broadening of the peak is further verified by the increase in full width at half maxima (FWHM) of the plot as the content of respective metal oxide increases. The most significant magnetic entropy drop from the pure LCMO is seen in LCMO-5%NiO. The entropy drops from 8.77 $JKg^{-1}K^{-1}$ in pure LCMO to 3.24 $JKg^{-1}K^{-1}$ in LCMO-5%NiO. The most significant increase in full-width at half maxima (FWHM) of the plot is for the LCMO-5%CoO sample. The FWHM increases from 24.63 K in pure LCMO to 64.09 K in LCMO-5%CoO. This gives us the operational temperature for the samples, which has increased significantly high for LCMO-5%CoO. This increase in FWHM is observed in smaller amounts in other samples but is still significant, improving the practical application. The decrease in ΔS_{max} value is primarily attributed to the antiferromagnetic insulation of the LCMO by metal oxides [41, 43]. The magnetic inhomogeneity plays a significant role in both ΔS_{max} reduction and increase in FWHM value of the plot. Also, the volume fraction of the LCMO is decreased by increasing the metal oxide content. This decreases the fraction of ferromagnetic spins as compared to the pure sample [48].

Other than this, unintentional minor doping of metal ions on the B side of the LCMO perovskite replacing the Mn ions also can contribute to the reduction of ΔS_{max} **[35, 38, 42].**

Published literature show that the Mn ions in the Ca^{2+} substituted $LaMnO_3$ exhibiting double-exchange interaction. Mn ions exist in two different oxidation states, +3 and +4, due to the presence of La^{3+} and Ca^{2+} cations in the A-site [31, 32, 36, 37]. The magnetic Mn^{3+} and Mn^{4+} cations bonded through non-magnetic oxygen anion induce hopping of electrons in between these cations through oxygen to attain the least energy state. This is called double-exchange interaction. This phenomenon promotes ferromagnetic ordering. The replacement of such transition metal ions having the ability to exhibit different oxidation states by Ni^{2+}, Cu^{2+}, or Co^{2+} cations will minimize this delocalization of electrons and decrease the ferromagnetic ordering. Ultimately this yields a lower change in magnetic entropy.

Table 5.8. Maximum entropy change and FWHM of $La_{0.7}Ca_{0.3}MnO_3$-$xNiO$ ($x = 0.0\%$, 2.5%, 5.0%) at different applied fields.

Field(T)	$La_{0.7}Ca_{0.3}MnO_3$		$La_{0.7}Ca_{0.3}MnO_3$-2.5%NiO		$La_{0.7}Ca_{0.3}MnO_3$-5%NiO	
	ΔS_{max}	FWHM	ΔS_{max}	FWHM	ΔS_{max}	FWHM
1.0	4.75	8.86	3.14	14.14	1.05	29.12
2.0	6.61	13.31	4.62	20.38	1.74	33.68
3.0	7.54	17.36	5.22	27.18	2.30	38.50
4.0	8.23	21.14	5.74	33.93	2.79	43.12
5.0	8.77	24.63	6.16	39.45	3.24	47.10

Table 5.9. Maximum entropy change and FWHM of $La_{0.7}Ca_{0.3}MnO_3$-$xCuO$ ($x = 0.0\%$, 2.5%, 5.0%) at different applied fields.

Field(T)	$La_{0.7}Ca_{0.3}MnO_3$		$La_{0.7}Ca_{0.3}MnO_3$-2.5%CuO		$La_{0.7}Ca_{0.3}MnO_3$-5%CuO	
	ΔS_{max}	FWHM	ΔS_{max}	FWHM	ΔS_{max}	FWHM
1.0	4.75	8.86	2.45	19.79	2.12	25.75
2.0	6.61	13.31	3.59	26.73	3.32	32.47
3.0	7.54	17.36	4.39	32.30	4.02	39.11
4.0	8.23	21.14	5.05	37.12	4.58	46.05
5.0	8.77	24.63	5.59	41.72	5.02	53.14

Table 5.10. Maximum entropy change and FWHM of La$_{0.7}$Ca$_{0.3}$MnO$_3$-xNiO (x = 0.0%, 2.5%, 5.0%) at different applied fields.

Field(T)	La$_{0.7}$Ca$_{0.3}$MnO$_3$		La$_{0.7}$Ca$_{0.3}$MnO$_3$-2.5%CoO		La$_{0.7}$Ca$_{0.3}$MnO$_3$-5%CoO	
	ΔS_{max}	FWHM	ΔS_{max}	FWHM	ΔS_{max}	FWHM
1.0	4.75	8.86	2.47	19.70	1.18	42.18
2.0	6.61	13.31	3.92	26.45	2.02	52.30
3.0	7.54	17.36	4.75	32.20	2.69	58.04
4.0	8.23	21.14	5.36	37.49	3.26	61.72
5.0	8.77	24.63	5.87	42.85	3.75	64.09

Moreover, the file dependence of the maximum entropy change is given by equation (6). The exponent N was derived by fitting the experimental data at respective temperatures. Fig. 5.13shows the change in exponent N at different temperatures.
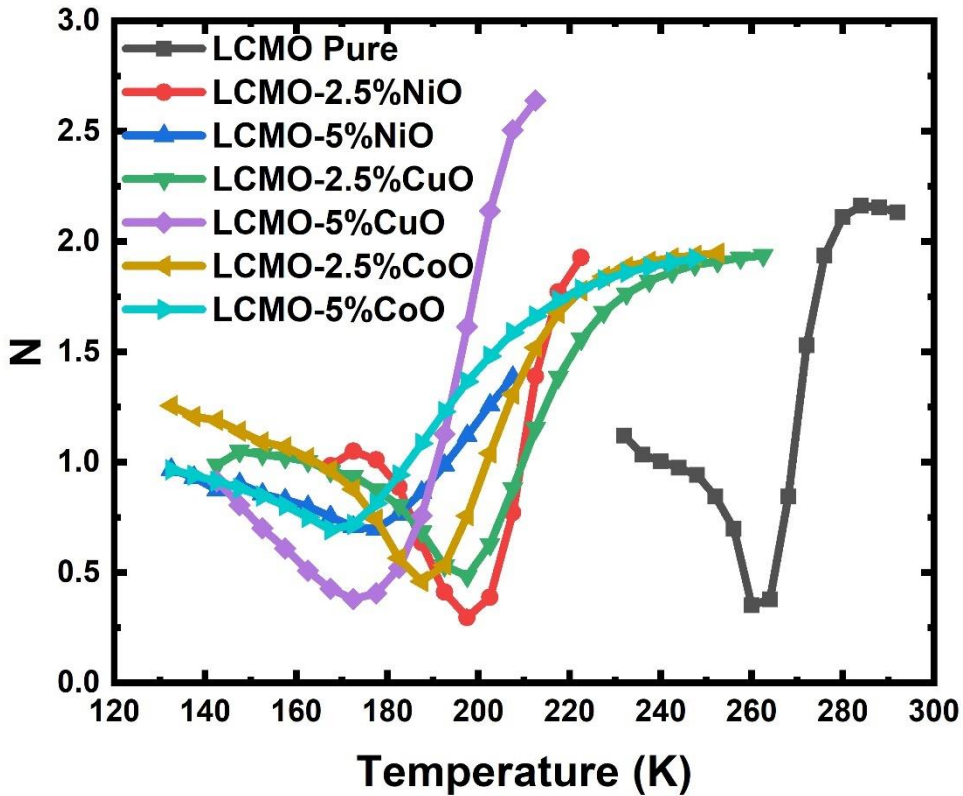
Fig. 5.13. Exponent N of La$_{0.7}$Ca$_{0.3}$MnO$_3$-x%MO (x = 0.0%, 2.5%, 5.0%) (M = Ni, Cu, Co) with respect to temperature.

We can see that the exponent N is minimum at the phase transition temperature (T_c) and exhibits smaller increase at temperatures below T_c and significant increase at temperatures above T_c which is expected [58]. Below T_c, the material is in ferromagnetic phase, so the magnetic entropy does not change as significantly due to external applied field whereas above T_c, the paramagnetic phase of the material is highly influenced by external applied field which significantly increases the N value.

The most important parameter to quantify the magnetocaloric property of a material is Relative Cooling Power (RCP). RCP is the amount of heat energy transferred in a complete ideal cycle of magnetic refrigeration. This accounts for the maximum change in entropy and the operational temperature of the given material as given mathematically by equation (7).

RCP was calculated using the data from Table 5.8, Table 5.9, and Table 5.10. Fig. 5.14 gives the RCP at different applied magnetic fields from 1-5 T. Table 5.11 also lists the RCP values for all the samples at different applied fields.
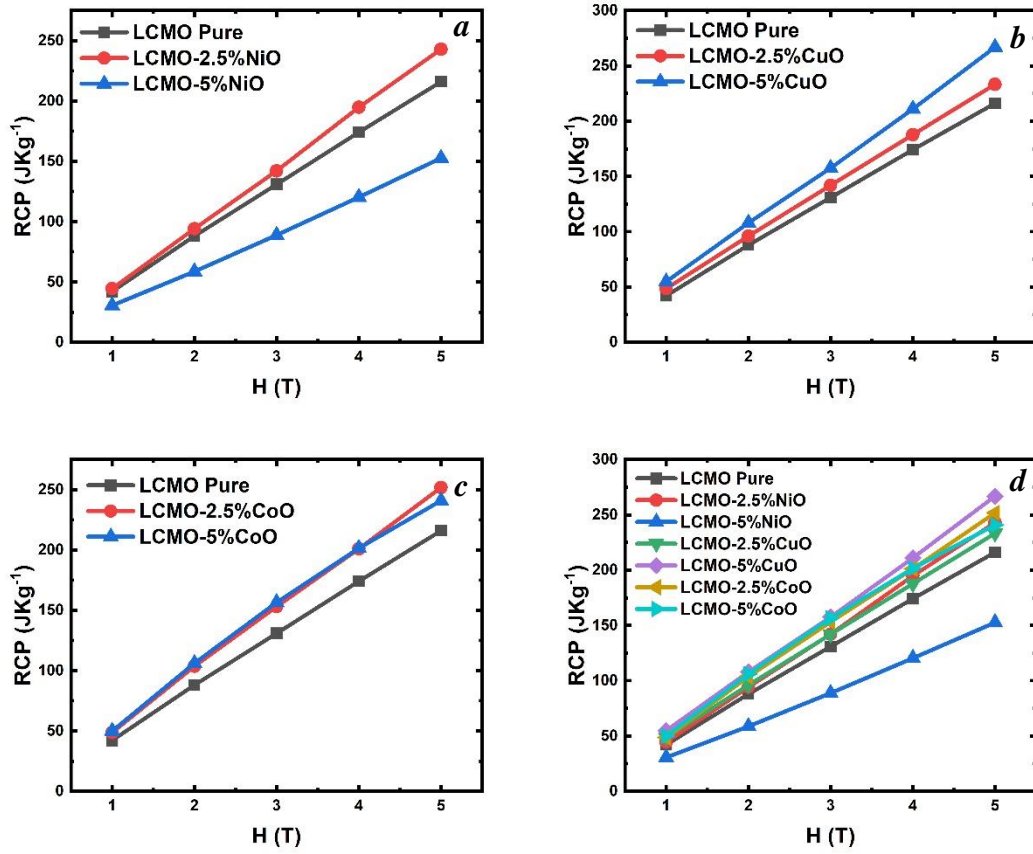
Fig. 5.14. RCP of a) La_{0.7}Ca_{0.3}MnO₃-x%NiO (x = 0.0%, 2.5%, 5.0%), b) La_{0.7}Ca_{0.3}MnO₃-x%CuO (x = 0.0%, 2.5%, 5.0%), c) La_{0.7}Ca_{0.3}MnO₃-x%CoO (x = 0.0%, 2.5%, 5.0%), and d) all combined with respect to applied field.

We observe that the RCP values increase with the increase in an applied magnetic field. This is due to the increase in entropy change with the increase in the field as a result of increasing ferromagnetic ordering, and RCP is linearly related to the change in entropy as given by the formula. The RCP of all composite samples has increased with respect to the pristine LCMO except for LCMO-5%NiO. The highest RCP value of 266.89 JKg^{-1} is observed in LCMO-5%CuO samples, which is 23.4% higher than 213.13 JKg^{-1} observed for the pure LCMO at an externally applied field of 5T. This is a substantial gain considering the decrease in ΔS_{max} values which is again attributed to the antiferromagnetic nature of the metal oxides giving rise to magnetic inhomogeneity [41, 43]. The loss in magnetic entropy change is compensated more than enough by broadening the peak, which increases the RCP. The

decrease in RCP for LCMO-5%NiO is because of the small increment in FWHM of the curve. This can be credited to the difference in phase transition temperature of the metal oxides with respect to that of LCMO [44]. The phase transition temperature for NiO is 525 K which is further away from 258 K for LCMO as compared to 230 K for CuO and 291 K for CoO. Due to this high difference in magnetic phase transition temperature, the RCP for a higher content of NiO in LCMO has dropped to 152.71 JKg^{-1}.

Table 5.11. RCP of La$_{0.7}$Ca$_{0.3}$MnO$_3$-x%MO (x = 0.0%, 2.5%, 5.0%) (M = Ni, Cu, Co) at different external applied fields.

Sample	RCP (J.Kg^{-1})				
	1T	2T	3T	4T	5T
La$_{0.7}$Ca$_{0.3}$MnO$_3$	42.15	88.07	130.93	174.21	216.12
La$_{0.7}$Ca$_{0.3}$MnO$_3$-2.5%NiO	44.51	94.19	142.17	194.92	243.05
La$_{0.7}$Ca$_{0.3}$MnO$_3$-5%NiO	30.58	58.75	88.83	120.41	152.71
La$_{0.7}$Ca$_{0.3}$MnO$_3$-2.5%CuO	48.62	96.15	142.02	187.77	233.37
La$_{0.7}$Ca$_{0.3}$MnO$_3$-5%CuO	54.85	107.97	157.51	211.12	266.89
La$_{0.7}$Ca$_{0.3}$MnO$_3$-2.5%CoO	48.79	103.76	153.25	201.16	251.78
La$_{0.7}$Ca$_{0.3}$MnO$_3$-5%CoO	50.04	106.15	156.66	201.52	240.88

Further, equation (9) is used to calculate the R values, through experimental fitting, which determines the sensitivity of RCP to the external applied field. The obtained data is shown in Table 5.12. We have seen small drops in R-value with composite formation for all samples except La$_{0.7}$Ca$_{0.3}$MnO$_3$-2.5%NiO. The drops are not significant though. All of them are fairly close to 1 which signifies that RCP has almost linear dependence with external applied field.

Table 5.12. R-value for La_{0.7}Ca_{0.3}MnO₃-x%MO (x = 0.0%, 2.5%, 5.0%) (M = Ni, Cu, Co).

Sample	R-value
$La_{0.7}Ca_{0.3}MnO_3$	1.0146
$La_{0.7}Ca_{0.3}MnO_3$-2.5%NiO	1.0558
$La_{0.7}Ca_{0.3}MnO_3$-5%NiO	0.999
$La_{0.7}Ca_{0.3}MnO_3$-2.5%CuO	0.9737
$La_{0.7}Ca_{0.3}MnO_3$-5%CuO	0.9775
$La_{0.7}Ca_{0.3}MnO_3$-2.5%CoO	1.0147
$La_{0.7}Ca_{0.3}MnO_3$-5%CoO	0.9805

Finally, the specific heat (C_p) of the samples is calculated from the ΔS_{max} vs T curve using equation (9).

Fig. 5.15 presents the specific heat values for the samples obtained at different values of the applied magnetic field from 1-5 T.
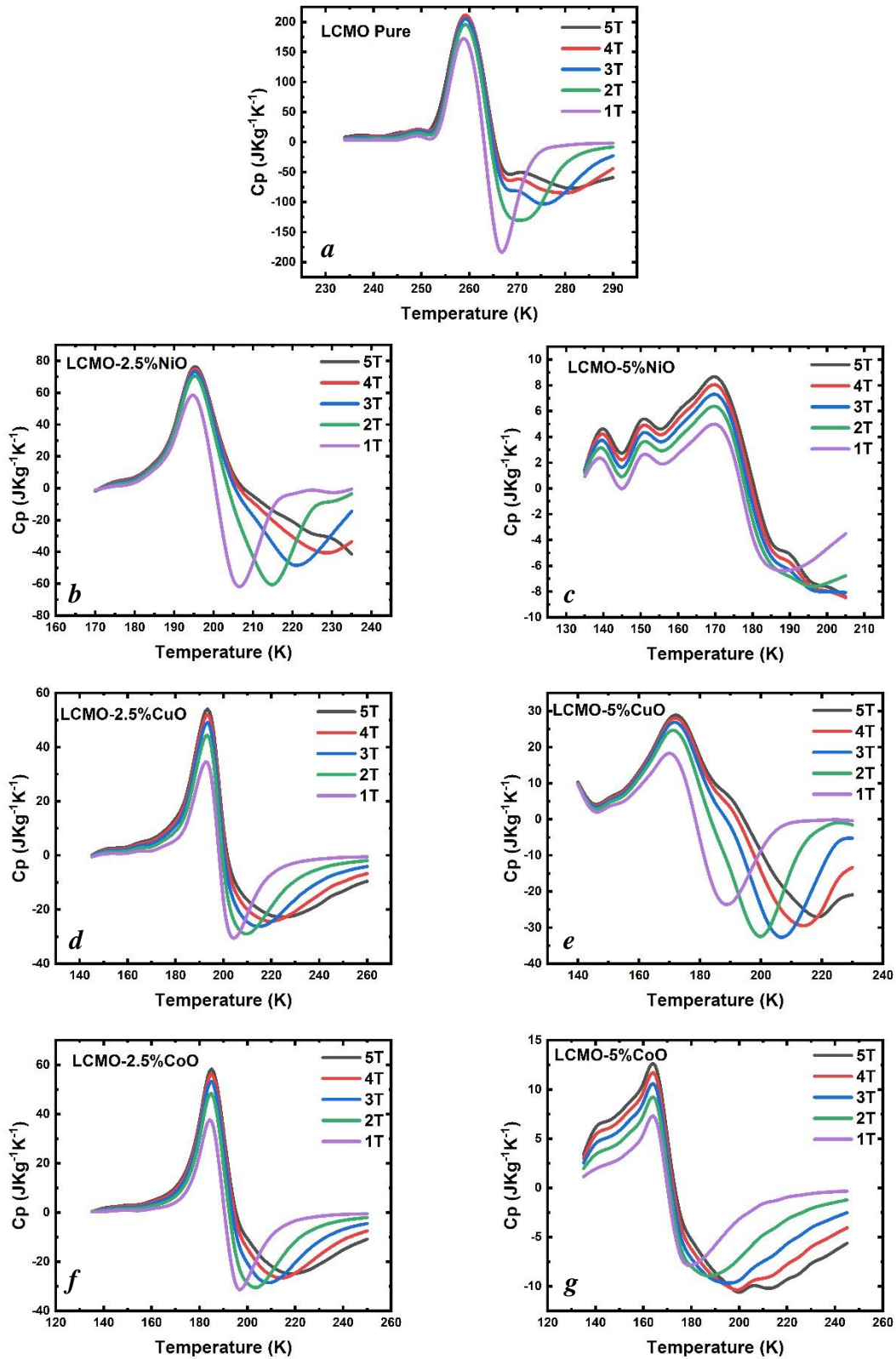
Fig. 5.15. Specific heat of a) La₀.₇Ca₀.₃MnO₃, b) La₀.₇Ca₀.₃MnO₃-2.5%NiO, c) La₀.₇Ca₀.₃MnO₃-5%NiO, d) La₀.₇Ca₀.₃MnO₃-2.5%CuO, e) La₀.₇Ca₀.₃MnO₃-5%CuO, f) La₀.₇Ca₀.₃MnO₃-2.5%CoO, and g) La₀.₇Ca₀.₃MnO₃-5%CoO at different applied fields.

We can see from the Fig. 5.15 that the specific heat value decreases with the decrease in temperature to a minimum value and suddenly rises to a maximum value around transition temperature. These values are the contribution to the specific heat of the sample due to magnetic entropy change. The maximum and minimum values for the magnetic entropy change's contribution to specific heat increases with the increase in the applied field as well. This contribution shows a decreasing trend with the increasing content of metal oxide. This means that the material's specific heat close to PM-FM transition temperature (T_c) is lowered with the increasing content of metal oxides. This increases the efficiency of the material as a refrigerant since low specific heat implies less energy required to bring change in temperature for the same mass of the material.

Table 5.13. Maximum and minimum specific heat of La$_{0.7}$Ca$_{0.3}$MnO$_3$-xMO (x = 0.0%, 2.5%, 5.0%) (M = Ni, Cu, Co) at 5T.

Sample	$C_{p\text{-}max}$	$C_{p\text{-}min}$
La$_{0.7}$Ca$_{0.3}$MnO$_3$	200.15	-77.26
La$_{0.7}$Ca$_{0.3}$MnO$_3$-2.5%NiO	76.26	-41.32
La$_{0.7}$Ca$_{0.3}$MnO$_3$-5%NiO	8.67	-8.41
La$_{0.7}$Ca$_{0.3}$MnO$_3$-2.5%CuO	50.54	-22.75
La$_{0.7}$Ca$_{0.3}$MnO$_3$-5%CuO	27.96	-26.7
La$_{0.7}$Ca$_{0.3}$MnO$_3$-2.5%CoO	58.30	-24.82
La$_{0.7}$Ca$_{0.3}$MnO$_3$-5%CoO	12.40	-10.14

Chapter 6 Conclusion

(1-x) $La_{0.7}Ca_{0.3}MnO_3$-*x*MO (*x = 0.0%, 2.5%, 5%*; M = Ni, Cu, Co) nanocomposites prepared using a simple autocombustion method were studied to examine structural and magnetic properties. The XRD, SEM, and EDS studies show that the sample exists in pure phase, and metal oxides do not react with LCMO but rather stay in the grain boundaries. The magnetic study shows that the sample undergoes PM-FM transition as we go to lower temperatures. The phase transition temperature (T_c) and ΔS_{max} decrease, whereas the RCP values increase with the increase in metal oxide content. The highest drop in T_c is recorded for LCMO-5%CoO with a drop of K. The largest loss of ΔS_{max} is seen in LCMO-5%NiO. The ΔS_{max} drops from in pure LCMO to in LCMO-5%NiO. There is a 23.4% gain in RCP observed for LCMO-5%CoO, which is the highest. These changes are primarily attributed to the magnetic inhomogeneity caused by the introduction of antiferromagnetic metal oxides in the grain boundaries of LCMO. The magnetic insulation and decrease in volume fraction of the LCMO play a role in decreasing the ferromagnetic ordering of the sample. Also, unintentional minor doping of metal ions in the Mn site of LCMO may impact the double exchange interaction.

Thus, with the RCP values of LCMO by the formation of metal oxides composites, we were able to enhance the magnetocaloric performance of the material. We were also able to interpret the nature of change in T_c with increasing metal oxide content.

Recommendation for Future Work

This work deals with the effect of composite formation of manganite with antiferromagnetic metal oxide in the magnetic properties. Further studies can be done with different nature of materials instead of the primary manganites or antiferromagnetic metal oxides to isolate the observed phenomena and effects. Different types of manganites such as $La_{1-x}Sr_xMnO_3$ can be tested to see if the results can be duplicated to explore any other underlying phenomenon. Also, autocombustion method was used during synthesis. Some unwanted doping of metal ions on the Mn site was suspected. Different synthesis techniques can be acquired to omit this unwanted doping.

References

1. D. Jiles. "Introduction to magnetism and magnetic materials". *CRC press* (2015).

2. B. Issa, I.M. Obaidat, R.H. Hejasee, S. Qadri, and Y. Haik. "Magnetic nanoparticles: surface effects and properties related to biomedicine applications." *International Journal of Molecular Sciences* **14**, (2013): 21266-21305.

3. D. Tarling, and F. Hrouda. "Magnetic Anisotropy of Rocks." *Chapman and Hall* (1993).

4. E. Warburg. "The thermodynamics of phase equilibrium." *Annals of Physics* **13**, no. 1 (1881).

5. P. Debye. "Zerstreuung von Röntgenstrahlen." *Annals of Physics* **81** (1926): 1154.

6. W.F. Giauque. "A Thermodynamic treatment of certain magnetic effects. A proposed method of producing temperatures considered below 1° absolute." *Journal of American Chemical Society* **49** (1927): 1864.

7. E. Brück. "Developments in magnetocaloric refrigeration." *Journal of Physics D: Applied Physics* **38**, no. 23 (2005): R381.

8. G.F. Wang, L.R. Li, Z.R. Zhao, X.Q. Yu, and X.F. Zhang. "Structural and magnetocaloric effect of $Ln_{0.67}Sr_{0.33}MnO_3$ (Ln=La, Pr and Nd) nanoparticles." *Ceramics International* **40**, no. 10 (2014): 16449-16454.

9. Y. Liu, F.R. Shen, M. Zhang, L.F. Bao, R.R. Wu, Y.Y. Zhao, F.X. Hu, J. Wang, W.L. Zuo, J.R. Sun, and B.G. Shen. "Stress modulated martensitic transition and magnetocaloric effect in hexagonal Ni_2In-type MnCoGe1−xInx alloys." *Journal of Alloys and Compounds* **649** (2015): 1048-1052.

10. E. Yüzüak, I. Dincer, Y. Elerman, I. Dumkow, B. Heger, and S. Yuce Emre. "Enhancement of magnetocaloric effect in $CoMn_{0.9}Fe_{0.1}Ge$ alloy." *Journal of Alloys and Compounds* **641** (2015): 69-73.

11. S.N. Dembele, Z. Ma, Y.F. Shang, H. Fu, E.A. Balfour, R.L. Hadimani, D.C. Jiles, B.H. Teng, and Y. Luo. "Large magnetocaloric effect of $GdNiAl_2$ compound." *Journal of Magnetism and Magnetic Materials* **391** (2015): 191-194.

12. Z. Li, Y.L. Zhang, K. Xu, and C. Jing. "Large magnetocaloric effect related to martensitic transformation in $Ni_{50}Co_2Mn_{33}In_{15}$ textured alloy." *Physica B: Condensed Matter* **476** (2015): 179-182.

13. C.L. Zhang, H.F. Shi, E.J. Ye, Y.G. Nie, Z.D. Han, and D.H. Wang. "Magnetostructural transition and magnetocaloric effect in MnCoGe–NiCoGe system." *Journal of Alloys and Compounds* **639** (2015): 36-39.

14. X. Chen, and R.V. Ramanujan. "Large magnetocaloric effect near room temperature in Mn–Fe–P–Ge nanostructured powders." *Journal of Alloys and Compounds* **652** (2015): 393-399.

15. Z. Mo, J. Shen, L. Li, Y. Liu, C. Tang, F. Hu, J. Sun, and B. Shen. "Observation of giant magnetocaloric effect in $EuTiO_3$." *Materials Letters* **158** (2015): 282-284.

16. M. Balli, B. Roberge, J. Vermette, S. Jandl, P. Fournier, and M.M. Gospodinov. "Magnetocaloric properties of the hexagonal $HoMnO_3$ single crystal revisited." *Physica B: Condensed Matter* **478** (2015): 77-83.

17. A. Jerbi, A. Krichene, N. Chniba-Boudjada, and W. Boujelben. "Magnetic and magnetocaloric study of manganite compounds $Pr_{0.5}A_{0.05}Sr_{0.45}MnO_3$ (A=Na and K) and composite." *Physica B: Condensed Matter* **477** (2015): 75-82.

18. A. Mleiki, S. Othmani, W. Cheikhrouhou-Koubaa, M. Koubaa, A. Cheikhrouhou, and E.K. Hlil. "Effect of praseodymium doping on the structural, magnetic and magnetocaloric properties of $Sm_{0.55}Sr_{0.45}MnO_3$ manganite." *Solid State Communications* **223** (2015): 6-11.

19. M. Mansouri, H. Omrani, W. Cheikhrouhou-Koubaa, M. Koubaa, A. Madouri, and A. Cheikhrouhou. "Effect of vanadium doping on structural, magnetic and magnetocaloric properties of $La_{0.5}Ca_{0.5}MnO_3$." *Journal of Magnetism and Magnetic Materials* **401** (2016): 593-599.

20. S. Chandra, A. Biswas, M. Phan, and H. Srikanth. "Impacts of nanostructuring and magnetic ordering of Nd^{3+} on the magnetic and magnetocaloric response in $NdMnO_3$." *Journal of Magnetism and Magnetic Materials* **384** (2015): 138-143.

21. A., S. Chandra, M. Phan, and H. Srikanth. "Magnetocaloric properties of nanocrystalline LaMnO3: Enhancement of refrigerant capacity and relative cooling power." *Journal of Alloys and Compounds* **545** (2012): 157-161.

22. H. Yang, Y.H. Zhu, T. Xian, and J.L. Jiang. "Synthesis and magnetocaloric properties of $La_{0.7}Ca_{0.3}MnO_3$ nanoparticles with different sizes." *Journal of Alloys and Compounds* **555** (2013): 150-155.

23. E. Pavarini, and E. Koch. "Origin of Jahn-Teller Distortion and Orbital Order in $LaMnO_3$." *Physical Review Letter* **104**, no. 8 (2010): 086402.

24. M. Iqbal, M.N. Khan, and A.A. Khan. "Structural, magnetic, magnetocaloric and critical behavior studies in the vicinity of the paramagnetic to ferromagnetic phase transition temperature in $LaMnO_{3+\delta}$ compound." *Journal of Magnetism and Magnetic Materials* **465** (2018): 670-677.

25. P.S. Tola, D.H. Kim, T.L. Phan, C. Liu, and B.W. Lee. "Magnetic properties and magnetocaloric effect of $LaMnO_3$ nanoparticles prepared by using the sol-gel method." *Journal of the Korean Physical Society* **69** (2016): 65–71.

26. V. Dyakonov, W. Bazela, R. Duraj, M. Dul, Z. Kravchenko, K. Dyakonov, S. Baran, A. Szytula, and H. Szymczak. "Grain size effect on magnetic properties of $REMnO_3$ (RE=Pr, Nd)." *Low Temperature Physics* **39** (2013): 351.

27. A. Midya, S. N. Das, P. Mandal, S. Pandya, and V. Ganesan. "Anisotropic magnetic properties and giant magnetocaloric effect in antiferromagnetic $RMnO_3$ crystals (R=Dy, Tb, Ho, and Yb)." *Physics Review B* **84** (2011): 235127.

28. M. Balli, S. Mansouri, S. Jandl, P. Fournier, and D.Z. Dimitrov. "Large rotating magnetocaloric effect in the orthorhombic DyMnO3 single crystal." *Solid State Communications* **239** (2016): 9-13.

29. M. Balli, P. Fournier, S. Jandl, S. Mansouri, A. Mukhin, Yu. V. Ivanov, and A. M. Balbashov. "Comment on Giant anisotropy of magnetocaloric effect in $TbMnO_3$ single crystal." *Physics Review B* **96** (2017): 146401.

30. N. Kumar Swamy, N. Pavan Kumar, P.V. Reddy, M. Gupta, S.S. Samatham, D. Venkateshwarulu, V. Ganesan, V. Malik, and B.K. Das. "Specific heat and magnetocaloric effect studies in multiferroic $YMnO_3$." *Journal of Thermal Analysis and Calorimetry* **119** (2015): 1191–1198.

31. R. Das, A. Idya, M. Kumari, A. Chaudhuri, X. Yu, A. Rusydi, and R. Mahendiran. "Enhanced Magnetocaloric Effect Driven by Hydrostatic Pressure in Na-Doped $LaMnO_3$." *The Journal of Physical Chemistry C* **123**, no. 6 (2019): 3750-3757.

32. M.S. Afify, M.M. El Faham, U. Eldemerdash, W.M.A. El Rouby, and S.I. El-Dek. "Room temperature ferromagnetism in Ag doped $LaMnO_3$ nanoparticles." *Journal of Alloys and Compounds* **861** (2021): 158570.

33. V.S. Kolat, S. Atalay, T. Izgi, H. Gencer, and H. Bayri. "Structural, Magnetic, and Magnetocaloric Properties of $La_{1-x}Bi_xMnO_3$ ($x = 0.01, 0.03, 0.06, 0.1, 0.2$) Compounds." *Metallurgical and Materials Transactions A* **46** (2015): 2591–2597.

34. N. Kallel, S. Kallel, A. Hagaza, and M. Oumezzine. "Magnetocaloric properties in the Cr-doped $La_{0.7}Sr_{0.3}MnO_3$ manganites." *Physica B: Condensed Matter* **404**, no. 2 (2009): 285-288.

35. T.L. Phan, P.Q. Thanh, P.D.H. Yen, P. Zhang, T.D. Thanh, and S.C. Yu. "Ferromagnetic short-range order and magnetocaloric effect in Fe-doped $LaMnO_3$." *Solid State Communications* **167** (2013): 49-53.

36. Z. Ur Rehman, M.S. Anwar, and B.H. Koo. "Influence of Barium Doping on the Magnetic and Magnetocaloric Properties of $Pr_{1-x}Ba_xMnO_3$." *Journal of Superconductivity and Novel Magnetism* **28** (2015): 1629–1634.

37. B. Biswas, S. Taran, and S. Pal. "Study of magnetocaloric properties in monovalent doped $Pr_{0.75}Li_{0.25}MnO_3$." AIP Conference Proceedings 2352, (2021): 020016.

38. S. Hcini, M. Boudard, S. Zemni, and M. Oumezzine. "Effect of Fe-doping on structural, magnetic and magnetocaloric properties of $Nd_{0.67}Ba_{0.33}Mn_{1-x}Fe_xO_3$ manganites." *Ceramics International* **40**, no. 10 (2014): 16041-16050.

39. M. Baazaoui, M. Boudard, and S. Zemni. "Magnetocaloric properties in $Ln_{0.67}Ba_{0.33}Mn_{1-x}Fe_xO_3$ (Ln=La or Pr) manganites." *Materials Letters* **65**, no. 14 (2011): 2093-2095.

40. A. El Boukili, O. Mounkachi, M. Hamedoun, P. Lachkar, E.K. Hlil, A. Benyoussef, M. Balli, and H. Ez-Zahraouy. "A study of structural, magnetic and magnetocaloric properties of $(1-x)La_{0.6}Ca_{0.4}MnO_3/xMn2O3$ composite materials." *Journal of Alloys and Compounds* **859** (2021): 158392.

41. M.S. Anwar, F. Ahmed, R. Danish, and B.H. Koo. "Impact of Co3O4 phase on the magnetocaloric effect and magnetoresistance in $La_{0.7}Sr_{0.3}MnO_3/Co_3O_4$ and $La_{0.7}Ca_{0.3}MnO_3/Co_3O_4$ ceramic composites." *Ceramics International* **41**, no. 1 (2015): 631-637.

42. M. Nasri, J. Khelifi, J. Laifi, F. Hcini, B. Alzahrani, M.L. Bouazizi, E. Dhahri, and E.K. Hlil. "Structural, magnetic and theoretical investigation of the magnetocaloric

effect of $La_{0.6}Sr_{0.4}MnO_3/x(Sb_2O_3)$ compound." *Phase Transitions* **94**, no. 3-4 (2021): 170-182.

43. T.P. Gavrilova, I.F. Gilmutdinov, J.A. Deeva, T.I. Chupakhina, N.M. Lyadov, I.A. Faizrakhmanov, F.O. Milovich, Yu.V. Kabirov, and R.M. Eremina. "Magnetic and magnetocaloric properties of $(1-x)$ $La_{0.7}Sr_{0.3}MnO_3/xNaF$ composites." *Journal of Magnetism and Magnetic Materials* **467** (2018): 49-57.

44. D. Neupane, L. Hulsebosch, A. K. Pathak and S. R. Mishra, "Magnetocaloric Study of $La_{0.45}Nd_{0.25}Sr_{0.3}MnO_3/MO$ (MO=CuO, CoO, and NiO) Nanocomposites." *IEEE Transactions on Magnetics* (2021).

45. K. El Maalam, M. Balli, S. Habouti, M. Dietze, M. Hamedoun, E.-K. Hlil, M. Es-Souni, A. El Kenz, A. Benyoussef, and O. Mounkachi. "Composite $(La_{0.45}Nd_{0.25})Sr_{0.3}MnO_3/5CuO$ materials for magnetic refrigeration applications." *Journal of Magnetism and Magnetic Materials* **449** (2018): 25-32.

46. A. Ezaami, N. Ouled Nasser, W. Cheikhrouhou-Koubaa, and A. Cheikhrouhou. "Enhancement of magnetocaloric properties in $(1-x)$ $La_{0.7}Ca_{0.2}Sr_{0.1}MnO_3/xLa_{0.7}Ca_{0.15}Sr_{0.15}MnO_3$ composite system ($0 \leq x \leq 1$)." *Materials Research Bulletin* **95** (2017): 211-215.

47. R. M'nassri, N.Chniba Boudjada, and A. Cheikhrouhou. "Nearly constant magnetic entropy change involving the enhancement of refrigerant capacity in $(La_{0.6}Ba_{0.2}Sr_{0.2}MnO_3)(1-x)/(Co_2O_3)x$ composite." *Ceramics International* **42**, no. 6 (2016): 7447-7454.

48. A.M. Ahmed, H.F. Mohamed, A.K. Diab, and Esraa Y. Omar. "Crossover effect of magnetotransport and magnetocaloric effect in $(La_{0.7}Ba_{0.3}MnO_3)(1-x)/(Al_2O_3)x$ composites." *Journal of Magnetism and Magnetic Materials* **489** (2019): 165388.

49. A.M. Ahmed, H.F. Mohamed, J.A. Paixão, and Sara A. Mohamed. "Thermopower and magnetocaloric properties in NdSrMnO/CrO$_3$ composites." *Journal of Magnetism and Magnetic Materials* **456** (2018): 217-222.

50. L. Fkhar, O. Mounkachi, K. El Maalam, M. Hamedoun, A. Mahmoud, F. Boschini, A. El Kenz, M.A. Ali, E.K. Hlil, Y. Xiao, and A. Benyoussef. "Large Magnetic Entropy Change in Pr$_{2/3}$Sr$_{1/3}$MnO$_3$-CuO Composite at Room Temperature." *Journal of Superconductivity and Novel Magnetism* **32** (2019): 3579–3585.

51. S. Specchia, C. Galletti, and V. Specchia. "Solution Combustion Synthesis as intriguing technique to quickly produce performing catalysts for specific applications." *Studies in Surface Science and Catalysis* **175** (2010): 59-67.

52. S.T. Aruna. "Concise Encyclopedia of Self-Propagating High-Temperature Synthesis." *Elsevier Science* (2017).

53. S.T. Aruna, and A.S. Mukasyan. "Combustion Synthesis and Nanomaterials." *Current Opinion in Solid State and Materials Science* **12** (2008): 44-50.

54. B.K. Banerjee. "On a generalized approach to first and second order magnetic transitions." *Physics Review Letters* **12**, no. 1 (1964): 16-17.

55. K.H. Wu, Y.C. Chang, and G.P. Wang. "Preparation of NiZn ferrite/SiO$_2$ nanocomposite powders by sol–gel auto-combustion method." *Journal of Magnetism and Magnetic Materials* **69**, no. 2 (2004): 150-155.

56. K. Vignesh, R. Priyanka, M. Rajarajan, and A. Suganthi. "Photoreduction of Cr(VI) in water using Bi$_2$O$_3$–ZrO$_2$ nanocomposite under visible light irradiation." *Material Science and Engineering B* **178** (2013): 149-157.

57. W. Tang, W. Lu, X. Luo, B. Wang, X. Zhu, W. Song, Z. Yang, and Y. Sun. "Particle size effects on La$_{0.7}$Ca$_{0.3}$MnO$_3$: size-induced changes of magnetic phase transition

order and magnetocaloric study." *Journal of Magnetism and Magnetic Materials* **322**, no. 16 (2010): 2360-2368.

58. M. Pekala. "Magnetic field dependence of magnetic entropy change in nanocrystalline and polycrystalline manganites La$_{1-x}$M$_x$MnO$_3$ (M = Ca, Sr)." *Journal of Applied Physics* **108** (2010): 113913.